ISSN 0234-5366

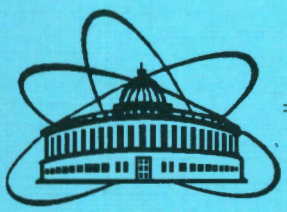

КРАТКИЕ СООБЩЕНИЯ ОИЯИ

JINR RAPID COMMUNICATIONS

3[83]-97

Издательский отдел ОИЯИ ДУБНА

JINR Publishing Department DUBNA

Объединенный институт ядерных исследований
Joint Institute for Nuclear Research

3[83]-97

КРАТКИЕ СООБЩЕНИЯ ОИЯИ

JINR RAPID COMMUNICATIONS

Дубна 1997

ОГЛАВЛЕНИЕ
CONTENTS

УДК 539.12...14

OBSERVATION OF TRANSVERSAL HANDEDNESS IN THE DIFFRACTIVE PRODUCTION OF PION TRIPLES

A.V.Efremov,[1] *Yu.I.Ivanshin*[2], *L.G.Tkatchev*[3], *R.Ya.Zulkarneev*[2]

A rather large, transversal to the production plane, handedness was observed in coherent production of $(\pi^-\pi^+\pi^-)$ triples by 40 GeV π^--beam on nuclei.

Наблюдение поперечной спиральности пионных троек при дифракционном рождении

А.В.Ефремов и др.

Для когерентно рожденных на ядре пионных троек $(\pi^-\pi^+\pi^-)$ 40 ГэВ π^--пучком наблюдена значительная, поперечная к плоскости рождения, спиральность этих троек.

Some years ago the concept of jet handedness was introduced as a measure of polarization of parent partons (or hadrons) [1]. For strong interaction process, parity invariance requires that at least three particles (spinless or spin averaged) in final state or the pair of particles and jet direction were measured in order to have a correlation in the fragmentation (or decay) distribution with initial helicity. Namely, from three particle momenta one can construct a pseudovector $n_\mu \propto \varepsilon_{\mu\nu\sigma\rho} k_1^\nu k_2^\sigma k^\rho$ $(k = k_1 + k_2 + k_3)$ which gives, when contracted with the initial polarization pseudovector, a scalar component in the strong process. Thus measuring the asymmetry (handedness) in some component of **n** in the rest frame of the triple and averaging over the other component can give information on the initial polarization in this direction

$$H_i = \frac{N(n_i > 0) - N(n_i < 0)}{N(n_i > 0) + N(n_i < 0)} = A_i P_i, \qquad (1)$$

[1]Bogoliubov Laboratory of Theoretical Physics, JINR, Dubna.
[2]Laboratory of Particle Physics, JINR, Dubna.
[3]Laboratory of Nuclear Problems, JINR, Dubna.

providing the analysing power A is large enough. The direction i could be chosen as longitudinal (L) with respect to the triple momentum $\mathbf{k}$ as transversal ones ($T1$ or $T2$) perpendicular to the triple production plane or in the plane[1]. It was argued [1] that for jet fragmentation process the longitudinal and transversal analysing power could be of different value while for a three-particle decay they are equal.

The longitudinal handedness was first probed in $e^+e^- \to Z \to q\bar{q} \to$ 2-jet process [5], where quarks are longitudinally polarized due to interference of the vector and axial coupling. The best result of measurement was $H^{e^+e^-} = (1.2 \pm 0.5)\%$ seen for leading $(++-)$ and $(--+)$ pion triples in the ρ-resonance region of invariant mass of $(+-)$-pairs. The SLD result [6] obtained with a polarized electron beam is $H < 2\%$. Also the correlation of longitudinal handedness in two-jet events was investigated [7] giving a puzzling sign contradicting to the CP-conjugation of the two jets and to factorization of q and $\bar{q}$ fragmentation functions.

In this paper we present the first probe for measuring the *transversal* handedness in the diffractive hadron process [8]

$$\pi^- + A \to (\pi^-\pi^+\pi^-) + A, \tag{2}$$

where A is for Be, Si and Pb nuclei.

The direction of normal to the production plane of the pion triple was defined as

$$\mathbf{N} = (\mathbf{v}_{3\pi} \times \mathbf{v}_b), \tag{3}$$

where $\mathbf{v} = \mathbf{k}/\varepsilon$ are the velocities of initial π^--beam and final 3π-system in the Lab r.f. The direction of normal to the «decay plane» of the 3π-system was defined as

$$\mathbf{n} = (\mathbf{v}_f^- - \mathbf{v}^+) \times (\mathbf{v}_s^- - \mathbf{v}^+), \tag{4}$$

where $\mathbf{v}_{f(s)}^-$ or $\mathbf{v}^+$ are the velocities of fast (slow) π^- or π^+.

The handedness (1) for longitudinal component of $\mathbf{n}$

$$n_L = \mathbf{n}\cdot\mathbf{v}_{3\pi} \tag{5}$$

and two transversal components

$$n_{T1} = \mathbf{n}\cdot\mathbf{N} \text{ and } n_{T2} = \mathbf{n}\cdot(\mathbf{v}_{3\pi} \times \mathbf{N}) \tag{6}$$

were measured using about 10000 events for each of the targets. With no cut applied the result was as follows

$$\begin{aligned} &H_{T1}^{\mathrm{Be}} = 10.0 \pm 1.0\% \quad H_{T1}^{\mathrm{Si}} = 7.1 \pm 1.0\% \quad H_{T1}^{\mathrm{Pb}} = 6.5 \pm 1.0\% \\ &H_{T2}^{\mathrm{Be}} = -0.6 \pm 1.0\% \\ &H_{L}^{\mathrm{Be}} = 0.0 \pm 1.0\%. \end{aligned} \tag{7}$$

So, one can see that the only component allowed by parity conservation H_{T1} is different from zero and large enough.

[1] In fact an idea similar to the handedness was earlier proposed in works [2]. Its application to a certain heavy quark decays was studied in Ref.3. Similar technique was also studied in the work [4].

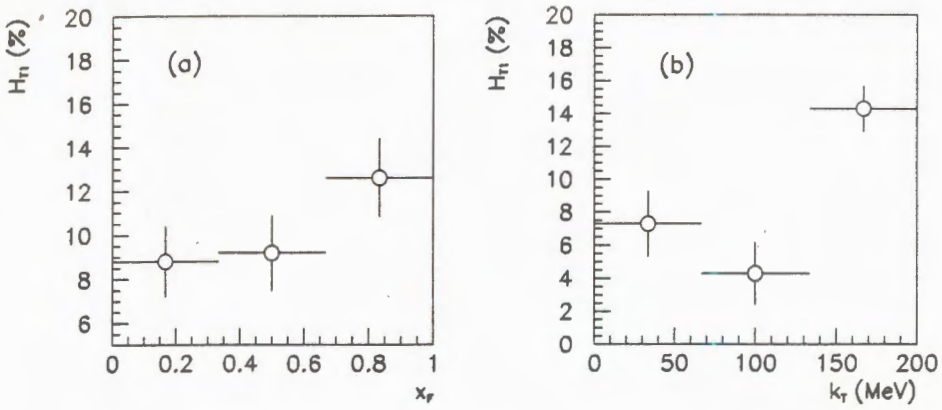

Fig. The handedness dependence on x_F (a) and k_T (b) for Be

The statistics permits one also to break the events into three bins in transversal momenta k_T of the triples or in fraction of longitudinal momentum $x_F = k_{Lf}/k_b$ of the fast π^-. The result of the binding for berillium target is presented in the Figure. It seems that some increase of the handedness value H_{T1} with increasing k_T or x_F is seen. This reminds a similar behaviour of Λ polarization or single spin pion asymmetry produced on a polarized target [9].

Trying to understand the reason of the phenomena, a cut was applied selecting events with the invariant mass of the triples in the region of a_1-resonance and invaruiant mass of each of the neutral pair in the region of ρ-meson. No noticeable change of the effect was observed after the cuts ($H_{T1} = 10.6 \pm 1.8\%$), just as for the cut of the neutral pairs invariant mass alone.

For convinction that the observed effect is not a consequence of some kinematics the Monte-Carlo events of reaction (2) were generated with a constant mass spectrum of the 3π-system in the interval 0.6—2.5 GeV/c^2 and with the experimental decrease with $t' = t - t_{min}$ of cross section with the slope 40 (Gev/c)$^{-2}$. The same selection of events with leading π^- shows no transversal handedness H_{T1} within the accuracy of 0.2%. Also no noticeable angular dependence of the normal **n** Expr. (4) was found both in earlier hydrogen bubble chamber data of reaction (2) at 4.5 GeV for the proton target and in the Regge pole exchange model which provides a reasonable description of that experiment [10].

In conclusion, rather large handedness transversal to the production plane was observed in the diffractive production of $(\pi^-\pi^+\pi^-)$ triples in the π^--beam fragmentation region. The physical reason for this phenomenon is far from clear. We are going to study the effect in more detail using more rich statistics.

The authors sincerely thank the participants of the Bologna-Dubna-Milan collaboration whose data were used in the present work. The work was partially supported by the Russian Foundation for Basic Research under the Grants 96-02-17936-a and 96-02-17631-a.

References

1. Efremov A., Mankiewicz L., Törnqvist N. — Phys. Lett., 1992, v.B284, p.394.
2. Nachtmann O. — Nucl. Phys., 1977, v.B127, p.314;
   Efremov A.V. — Sov. J. Nucl. Phys., 1978, v.28, p.83.
3. Dalitz R.H., Goldstein G., Marshall R. — Z. Phys., 1989, v.C42, p.441.
4. Collins J. — Nucl. Phys., 1993, v.B396, p.161;
   Collins J. et al. — Nucl. Phys., 1994, v.B420, p.565;
   Artru X., Collins J.C. — Z. Phys., 1996, v.C69, p.277.
5. Efremov A.V., Potashnikova I.K., Tkatchev L.G., Vertogradov L.S. — DELPHI 94-11 PHYS 355. 31 January 1994.
6. Abe K. et al. (SLD-Collaboration). — Phys. Rev. Lett., 1995, v.74, p.1512.
7. Efremov A.V., Potashnikova I.K., Tkatchev L.G. — Proc. Ranc. de Moriond, Meribel, 1994. See also 11th Int. Symp. on High Energy Spin Physics, Bloomington 1994, ISBN 1-56396-374-4, AIP Conf. Proc. 343 (1995) 821 and Proc. of 27th Int. Conf. on High Energy Physics, Glasgow 1994, (IOP, London, 1995) p.875;
   Bonivento W. et al. (DELPHI-Collaboration). — Report DELPHI 95-81 PHYS 516;
   Efremov A.V., Potashnikova I.K., Tkatchev L.G. — Proc. of Int. EPS Conf. on High Energy Physics, Brussels, 1995. See also JINR Commun. E1-95-417, Dubna, 1995. Proc. of 12th Int. Symp. on High Energy Spin Physics, Amsterdam, 1996.
8. Bellini G. et al. — Nucl. Phys., 1982, v.B199, p.433; Phys. Rev. Lett., 1982, v.48, p.1697; Let. Nuovo Cim., 1983, v.38, p.433; Nuovo Cim., 1984, v.A79, p.282.
9. See, e.g., talks of K.Heller and S.B.Nurushev in Proc. of 12th Int. Symp. on High Energy Spin Physics, Amsterdam, 1996.
10. Beketov G.V. et al. — Sov. J. Nucl. Phys., 1974, v.20, p.717 and 1975, v.22, p.525.

Received on April 30, 1997.

УДК 539.126.4

О ВОЗМОЖНОЙ ПОСТАНОВКЕ ЭКСПЕРИМЕНТА ПО ПОИСКУ ДИБАРИОННЫХ СОСТОЯНИЙ

В.В.Глаголев, Ю.Главачова[1], Н.Б.Ладыгина, Г.Мартинска[2], М.С.Ниорадзе[3], А.К.Качарава[3], Б.Пастирчак[4], Т.Семярчук[5], М.С.Хвастунов, Й.Урбан[2]

На основе анализа дейтрон-протонных взаимодействий в 100 см водородной пузырьковой камере ЛВЭ ОИЯИ выработан вариант постановки эксперимента по наблюдению дибарионных особенностей в эффективных массах двух протонов. Специальный выбор геометрии позволяет избавиться от большого фона квазиупругих столкновений. Сделаны оценки фона и скорости набора полезных событий.

Работа выполнена в Лаборатории высоких энергий ОИЯИ.

About a Possible Experiment on the Research of Dibaryon States

V.V.Glagolev et al.

The version of the experimental arrangement is proposed for the search of the dibaryon states in effective mass distribution of two protons. It was done on the ground of analysis of deuteron-proton interactions on the 100 cm hydrogen bubble chamber of the Laboratory of High Energies, JINR. The special geometry of experiment permits one to exclude a big background of the quasi-elastic scattering. The background and necessary yield for experiment have been estimated.

The investigation has been performed at the Laboratory of High Energies, JINR.

1. Введение

Несмотря на большое число экспериментов, в которых проявлялись особенности в поведении двухбарионных систем, факт наблюдения дибарионных резонансов пока не является общепризнанным. Мы не преследуем цели дать полный перечень про-

[1]Технический университет, Кошице, Словакия.
[2]Университет им. П.Й.Шафарика, Кошице, Словакия.
[3]Институт физики высоких энергий Тбилисского государственного университета, Грузия.
[4]Институт экспериментальной физики Словацкой академии наук, Кошице, Словакия.
[5]Институт ядерных исследований, Варшава.

водившихся исследований, т.к. существуют достаточно полные обзоры Б.Татищева [1], Ю.А.Трояна [2], других авторов. Большая часть экспериментов с наблюдением узких (экспериментальная ширина от 1 до 20 МэВ/c^2) особенностей была проведена в области промежуточных энергий. В частности, наблюдались особенности:

— в спектрах эффективных масс двух нуклонов в реакциях $dp \to (pp)n$ [3,4], $dp \to (pn)p$ [5], $np \to pp\pi^-$ [6], ^{4}He$p \to dppn$ [7], $\gamma d \to pp\pi^-$ [8] и других;

— в спектрах недостающих масс в реакциях $dp \to p\pi^+(nn)$ [5], ^{3}He$p \to dX$ [9];

— в поведении тензорной анализирующей способности в реакции ^{1}H(**d**, pp)X [10].

В упомянутых исследованиях преобладала методика пузырьковых камер, чаще — водородных (ОИЯИ, ЛИЯФ, КЕК), характеризуемая хорошими точностными характеристиками и позволяющая выделить отдельные реакции. Серьезный недостаток этой методики — большая трудоемкость обработки и ограниченные возможности по набору экспериментального материала. Отдельные эксперименты, выполненные электронной методикой, ставились не всегда адекватно задаче поиска дибарионов.

Сама же задача интересна и актуальна. Это видно хотя бы по серьезному отношению теоретиков, применявших и развивавших различные модели для объяснения феномена дибарионов. Обзор значительной части этих моделей сделан, например, в работе [11]. Наиболее близкими к наблюдаемому спектру масс дибарионов оказываются модели, рассматривающие возбуждения шестикварковых систем и квазиядерные системы (ΔN, $\Delta\Delta$). Появляются и нетрадиционные подходы [12,13].

Из сказанного следует вывод о том, что необходим систематический и целенаправленный поиск дибарионов (особенно узких) в экспериментах с большой статистикой и хорошим разрешением по массе.

2. Физические основания постановки эксперимента

Мы продемонстрируем одну из возможностей постановки эксперимента по исследованию спектра масс двух протонов в dp-взаимодействиях на ускорительном комплексе ОИЯИ. В своих оценках будем основываться на массиве около 200 тысяч обработанных дейтрон-протонных взаимодействий, полученных в условиях 4π-геометрии на 100 см водородной пузырьковой камере.

В первую очередь рассмотрим реакцию $dp \to ppn$. Другие реакции будут привлечены при оценках фона. В большинстве известных экспериментов исследовалась область эффективных масс двух нуклонов в диапазоне от 1,88 ГэВ/c^2 (сумма масс двух нуклонов) до 2,20 ГэВ/c^2. Мы будем придерживаться этого же диапазона. Эта область характерна тем, что включает в себя пороги рождения π-мезона и образования Δ-изобары ($2m_p + m_\pi \cong 2{,}02$ ГэВ/c^2 и $m_p + m_\Delta \cong 2{,}12$ ГэВ/c^2). Если предположить, что процессы с образованием шестикварковых систем идут на фоне виртуальных возбуждений двухбарионных систем (Δn, $\Delta\Delta$), то рационально работать при энергиях, соответствующих максимальному выходу изобар, т.е. в области импульсов дейтрона 3 + 4 ГэВ/с. В нашем случае, при $p_d = 3{,}34$ ГэВ/с, для квазинуклон-нуклонного столкновения $\sqrt{s} = 2{,}31$ ГэВ, что несколько выше порога рождения Δ-изобары, но поперечное сечение ее образования в этой области достигает максимума [14].

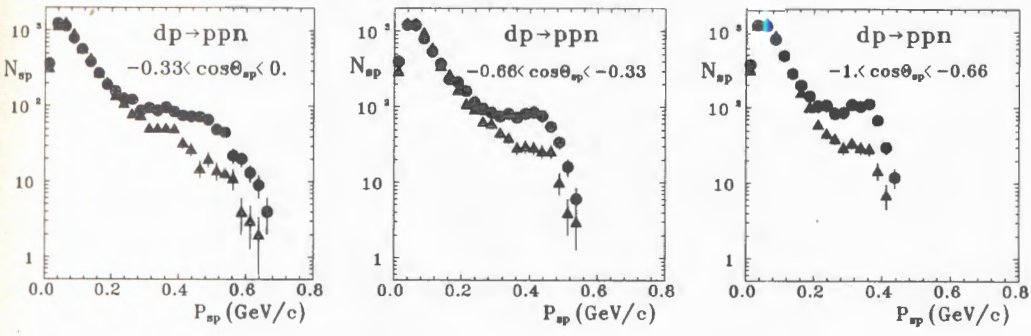

Рис.1. Импульсные спектры протонов (○)- и нейтронов (Δ)-спектаторов

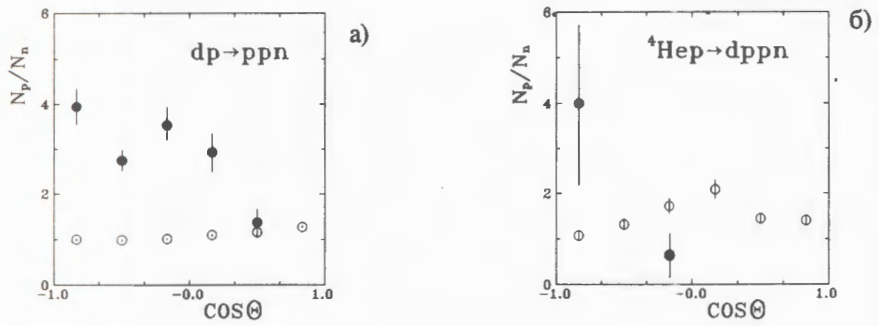

Рис.2. Зависимость отношения выходов протонов и нейтронов от угла вылета для реакций $dp \to ppn$ и $^4He p \to dppn$ для $x > 0{,}5$ (•) и $x < 0{,}5$ (○)

В реакции $dp \to ppn$ при $p_d = 3{,}34$ ГэВ/с эффекты, связанные с возбуждением виртуальной изобары, достаточно сильны [15]. Это можно видеть из сравнения спектров протонов и нейтронов, вылетающих в заднюю полусферу в системе покоя дейтрона (рис.1). Количественные оценки, сделанные на основе изотопических соотношений [16], показали, что в случае, если все события рассматриваемой реакции идут через возбуждение виртуальной Δ-изобары, отношение выхода протонов и нейтронов должно быть равно пяти. Тенденция такого поведения видна из рис.2а [17] для больших значений $x = T_{msx}/T$, где T — кинетическая энергия. На рис.2б приведены данные для отношения числа протонов и нейтронов в реакции $^4He p \to d_s ppn$ с дейтроном-спектатором [18]. Намечается аналогичное поведение этого отношения. Заметим, что в указанной реакции также наблюдались особенности в распределении по эффективным массам двух протонов. Реакция $^4He p \to d_s ppn$ сама выполняет роль фильтра, отбирающего «трехнуклонные» взаимодействия.

В реакции же $dp \to ppn$ подавляющим механизмом являются квазиупругое рассеяние и взаимодействие в конечном состоянии без изобарного возбуждения (треугольная

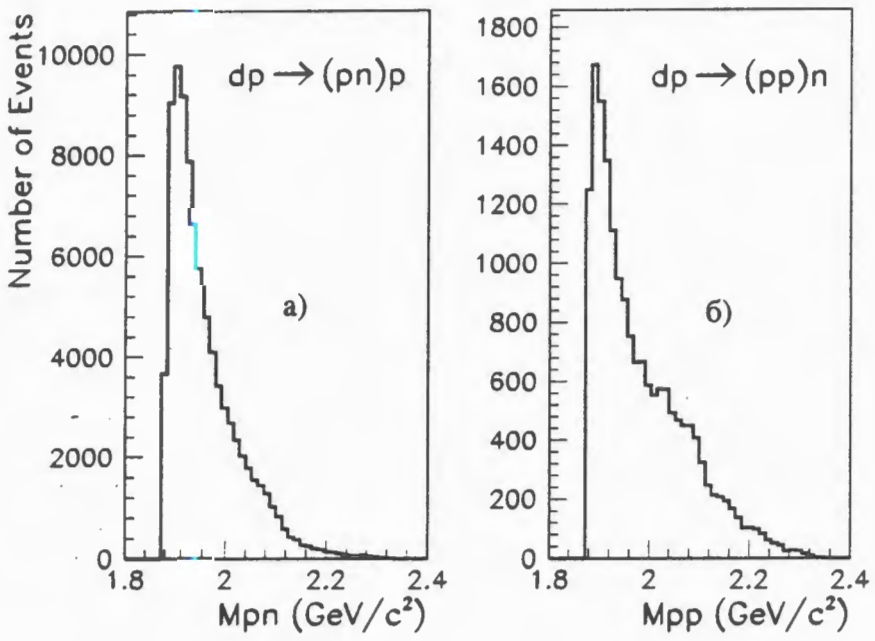

Рис.3. Распределения по эффективной массе протона и нейтрона (M_{pn}) в канале прямого развала дейтрона (а) и двух протонов (M_{pp}) в канале с перезарядкой (б)

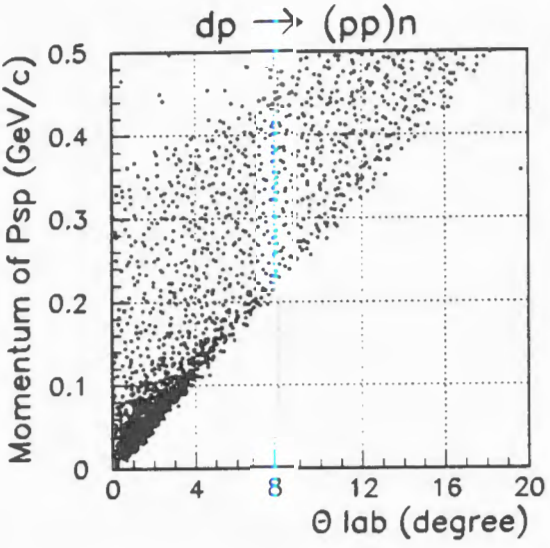

Рис.4. Зависимость импульсов протонов-спектаторов в системе покоя дейтрона от угла их вылета в лабораторной системе координат

диаграмма) [19]. Эти процессы сопровождаются обычно вылетом спектаторных нуклонов со спектром импульсов, хорошо описываемым большинством волновых функций дейтрона, без заметной высокоимпульсной части. Экспериментальные распределения (кроме нуклона отдачи в лабораторной системе координат) из таких событий имеют гладкий характер, без заметных особенностей. Эти распределения показаны на рис.3 отдельно для *pn*-комбинаций из канала прямого развала дейтрона $dp \to (pn)p$ (3а) и для *pp*-комбинаций развала с перезарядкой $dp \to (pp)n$ (3б). Под перезарядкой подразумеваются события, в которых нейтрон является лидирующей частицей в системе покоя дейтрона. Видно, что

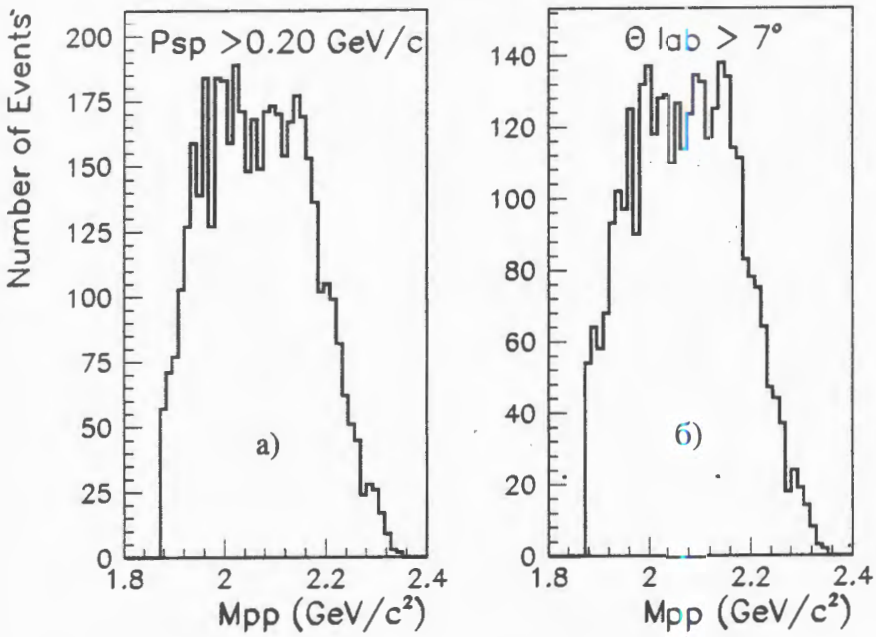

Рис.5. Спектры эффективных масс двух протонов из реакции $dp \to (pp)n$ при условиях: а) события с импульсом спектатора выше 0,20 ГэВ/с; б) события с углом вылета каждого из протонов $\Theta > 7°$

область больших M_{pp} (рис.3б) существенно обогащена событиями. Чтобы подавить фон от квазиупругих событий во многих экспериментах, например в [7], использовалось обрезание по импульсу спектатора. Для построения спектров M_{pp} брались только те события, в которых импульс протона-спектатора, т.е. самого медленного из нуклонов в системе покоя дейтрона, был больше некоторой величины, которая варьировалась в различных экспериментах в диапазоне 0,20 + 0,35 ГэВ/с. Это возможно сделать при эксклюзивной постановке опыта, когда выделяется реакция. На рис.4 представлено двумерное распределение зависимости импульса протона-спектатора в системе покоя дейтрона от угла его вылета в лабораторной системе координат для событий реакции $dp \to (pp)n$. Сгущение событий при малых p_s вблизи кинематической границы соответствует квазиупругому рассеянию. Выбирая события с $p_s > 0{,}20$ ГэВ/с, мы отбираем события более сложного типа. Это события с виртуальным возбуждением изобары, с потерей индивидуальности отдельных нуклонов ($6q$-мешки) и т.д. Результаты такого отбора показаны на рис.5а, где проявляется структура спектров M_{pp}, соответствующая наблюдаемым дибарионным особенностям. Вопрос заключается в том, как сделать аналогичный отбор в лабораторной системе координат, не выделяя конкретной реакции.

3. Постановка эксперимента

Из рис.4 видно, что благодаря сильной корреляции между p_s и Θ_{LAB} и наличию четкой конематической границы (кстати, она остается той же не только для спектаторов, но и для всех частиц) можно попытаться сделать обрезание по углу в лабораторной системе координат. В нашем случае импульсу $p_s = 0{,}20$ ГэВ/с соответствует угол $\Theta = 7°$. Теперь, если отберем только те события, в которых нет протонов, вылетающих под меньшим углом, получим M_{pp}-распределение, приведенное на рис.5б. Видно, что общий вид и детальная структура этого распределения практически совпадают с изображенными на рис.5а. Сделанное наблюдение является ключевым в нашем предложении. На его основе вырисовывается следующая схема опыта.

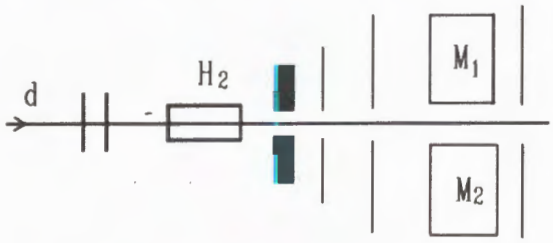

Рис.6. Схема эксперимента

Идеальной была бы конфигурация спектрометра, регистрирующего одновременный выход двух протонов, вылетающих в переднюю полусферу, за исключением конуса с раствором по полярному углу в $\Theta = 7°$ в случае импульса падающих дейтронов 3,34 ГэВ/с. При этом требуется измерение импульса протонов с максимально возможной точностью с целью улучшения разрешения по эффективной массе.

Более реальной выглядит схема, представленная на рис.6. Это — симметричный двухплечевой спектрометр с регистрацией двух протонов как в разных, так и в одном плече.

Можно обойтись и одним плечом. В этом случае несколько снижается эффективность регистрации событий в области больших масс M_{pp} (2,1 + 2,3 ГэВ/с^2).

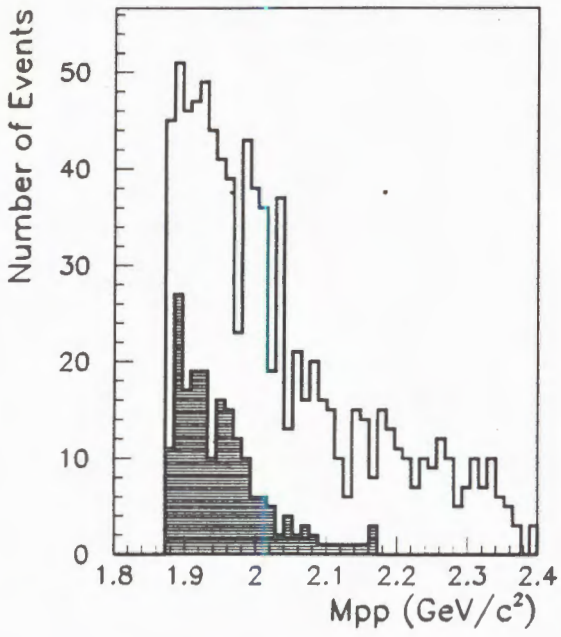

Рис.7. Спектр эффективных масс двух протонов из реакции $dp \to ppn$, у которых угол Θ лежит в интервале 7 + 30, а импульс — в интервале 1 + 2 ГэВ/с. Заштрихованная гистограмма — фон других реакций

Возникает вопрос о фоне от других реакций. Если ограничиться диапазоном импульсов вторичных протонов от 1,0 до 2,0 ГэВ/с, то убирается фон π-мезонов, импульс-

ный спектр которых не простирается выше 1,0 ГэВ/с. Например, не вносит вклада реакция $dp \to p\pi^+nn$, имеющая большое поперечное сечение. В асимметричном одноплечевом варианте полностью исключается влияние упругого dp-рассеяния.

В конкретном случае отбора пар положительно заряженных частиц с импульсом в диапазоне 1,0 ÷ 2,0 ГэВ/с и полярными углами Θ от 7 до 30° для одноплечевого варианта фоновые события представлены заштрихованной гистограммой на рис.7.

Используя полученные экспериментальные распределения, можно привести некоторые оценки по возможной скорости набора статистики. Так, для жидководородной мишени длиной 20 см и при потоке дейтронов на рабочую область мишени 10^6 в цикле ускорителя можно ожидать набора более 100000 полезных событий за 1—2 дня работы. Это означало бы увеличение статистики, набранной в экспериментах на водородных пузырьковых камерах для данной задачи, примерно в 1000 раз.

4. Заключение

Существование дибарионных резонансов продолжает оставаться в поле внимания экспериментаторов и теоретиков, надежное их обнаружение может способствовать дальнейшему продвижению в понимании свойств материи, таких, например, как кварковая структура ядерных объектов, конфайнмент.

Предложен один из возможных вариантов постановки эксперимента по наблюдению дибарионных резонансов. Оценки, проведенные на основе экспериментальных данных по дейтрон-протонным взаимодействиям, свидетельствуют о том, что эти исследования целесообразно проводить на дейтронных пучках ускорительного комплекса ЛВЭ ОИЯИ в области импульсов 3 ÷ 4 ГэВ/с.

Литература

1. Tatischeff B. — In: Proc. of the Xth Int. Sem. on High Energy Phys. Prob. (Ed. A.M.Baldin, V.V.Burov and L.P.Kaptari). Singapore, 1990, p.177.
2. Троян Ю.А. — ЭЧАЯ, 1993, т.24, в.3, с.683.
3. Dolidze M.G. et al. — Z. Phys., 1986, v.A325, p.391.
4. Andreev V.P. et. al. — Z. Phys., 1987, v.A327, p.434.
5. Балгансурен Я. и др. — ОИЯИ, Р1-88-503, Дубна, 1988.
6. Троян Ю.А. и др. — ОИЯИ, Д1-88-329, Дубна, 1988.
7. Glagolev V.V. et al. — Z. Phys., 1984, v.A317, p.335.
8. Böck B. et al. — Nucl. Phys., 1986, v.A459, p.573.
9. Tatischeff B. et al. — Nucl. Phys., 1985, v.A446, p.355.
10. Tatischeff B. et al. — Phys. Rev., 1992, v.C45, p.2005.
11. Лукьянов В.К., Титов А.И. — Изв. АН СССР, серия физ., 1990, т.54, №11, с.2082.
12. Ершов С.Н., Герасимов С.Б., Хрыкин А.С. — ЯФ, 1995, т.58, с.911.
13. Гареев Ф.А. — ОИЯИ, Р4-97-25, Дубна, 1997.
14. Ver West B.J., Arndt R.A. — Phys. Rev., 1982, v.C25, p.1979.

15. Aladashvili B.S. et al. — J. Phys. G: Nucl. Phys., 1997, v.3, p.1225.
16. Kopeliovich V.P. — Phys. Rep., 1986, v.139, p.2.
17. Глаголев В.В. и др. — ОИЯИ, Р1-12907, Дубна, 1979;
Glagolev V.V. — Nucl. Phys. (Proc. suppl.), 1994, v.B36, p.509.
18. Браун Г. и др. — ЯФ, 1996, т.59, с.2207.
19. Глаголев В.В. и др. — ЯФ, 1996, т.59, с.2001.

Рукопись поступила 9 апреля 1997 года.

УДК 539.1.074.4

CHERENKOV BEAM COUNTER SYSTEM OF THE CERES/NA45 SPECTROMETER FOR INVESTIGATION WITH 160 GeV/n.LEAD IONS

G.Agakichiev, A.Drees[1], *N.S.Moroz, Yu.A.Panebrattsev, S.V.Razin, N.Saveljic*[2], *S.S.Shimansky, G.P.Škoro*[3], *V.I.Yurevich*

Cherenkov beam counter system of the CERES/NA45 spectrometer was specially designed for experiments with 160 GeV/n lead ions of the SPS CERN. The counters provide a beam monitoring and a realization of a trigger of nucleus-nucleus collision in a target area. Construction scheme and main characteristics of the beam counters and also results of testing with lead beam are presented in this paper.

The investigation has been performed at the Laboratory of High Energies, JINR.

Система черенковских пучковых счетчиков спектрометра CERES/NA45 для исследований с 160 ГэВ/н.ионамн свинца

Г.Агакишиев и др.

Система черенковских пучковых счетчиков спектрометра CERES/NA45 была специально разработана для экспериментов с 160 ГэВ/н ионами свинца в ЦЕРН. Счетчики обеспечивают мониторирование пучка и реализацию триггера ядро-ядерного столкновения в области мишени. Представлены конструкция и основные характеристики пучковых счетчиков, а также результаты тестирования на пучке ядер свинца.

Работа выполнена в лаборатории высоких энергий ОИЯИ.

1. Introduction

One of the very important stages of the CERES/NA45 spectrometer modernization, with purpose to prepare and organize experiments with 160 GeV/n Pb-beam, was the elaboration of the beam counter (BC) system which main functions are contained in the following:

1. monitoring of the Pb-beam;

2. selection of the events with nucleus-nucleus collision in the target (interaction trigger);

[1]University of Heidelberg, Germany
[2]University of Montenegro, Yugoslavia
[3]INS «Vinca», Belgrade, Yugoslavia

3. time synchronization of trigger signals and readout of information from the slower main detectors of the spectrometer such as RICH (Ring Imaging Cherenkov) detectors, SIDC (Silicon Drift Chamber) and PC (Pad Chamber);

4. discrimination of the events with more than one Pb projectile within an active time of slower detectors, above mentioned, (before/after protection);

5. operative control of beam passage.

CERES is the experiment dedicated to the measurement of e^+e^- pairs and direct photons in nuclear collisions at SPS energies [1]. From this reason the basic requirement from BC system was minimization of the mass of constructive materials in the beam and target region, which could be potential source of background in measurements. The second, also important, requirement was the stability in the high radiation conditions.

Estimations had shown that for SPS beam structure and intensity of 10^6 nuclei/burst, absorption dose for plastic scintillator of BC would be about 4 Mrad for several days of working. There is well-known fact that for doses above such a value the light output of the scintillator rapidly decreases.

Therefore, BC system needs to provide good time and pulse height resolution and stable working conditions for the long time period (months) for the intensity of $n \cdot 10^6$ nuclei/burst. For realization of these requirements the new system of Cherenkov gaseous detectors, with extremely small mass along the beam path, was designed. Description of the detectors, construction properties, exploitation characteristics and the results of their testing with Pb beam are given bellow.

2. Method

In elaboration of the BC system for the CERES/NA45 spectrometer the following properties of Cherenkov radiation, induced by an ultrarelativistic lead nucleus passing through the gaseous radiator, have been used:

1. Energy of the Pb nucleus is much above the threshold energy for Cherenkov radiation for nitrogen/air radiator, under normal conditions ($E_{th} \simeq 38$ Gev/n);

2. Cherenkov radiation intensity is proportional to the charge squared of the particle and for Pb nucleus ($Z = 82$) there are many photons created per unit length even under the normal pressure;

3. Radiation propagates within a cone with a small angle relative to the beam axis ($\Theta_{max} \simeq 1.38°$ for air under normal conditions) that leads to an opportunity to collect Cherenkov photons, with high efficiency, on photocathode of photomultiplier tube (PMT) even with very small mirror.

The air at normal conditions has been used as a radiator in beam counters. The number of Cherenkov photons per unit length of radiator, within sensitivity range of PMT [λ_1, λ_2], is given by the well-known formula

$$\frac{dN}{dl} = 2\pi Z^2 \alpha \left(\frac{1}{\lambda_1} - \frac{1}{\lambda_2} \right) \cdot \sin^2 \Theta.$$

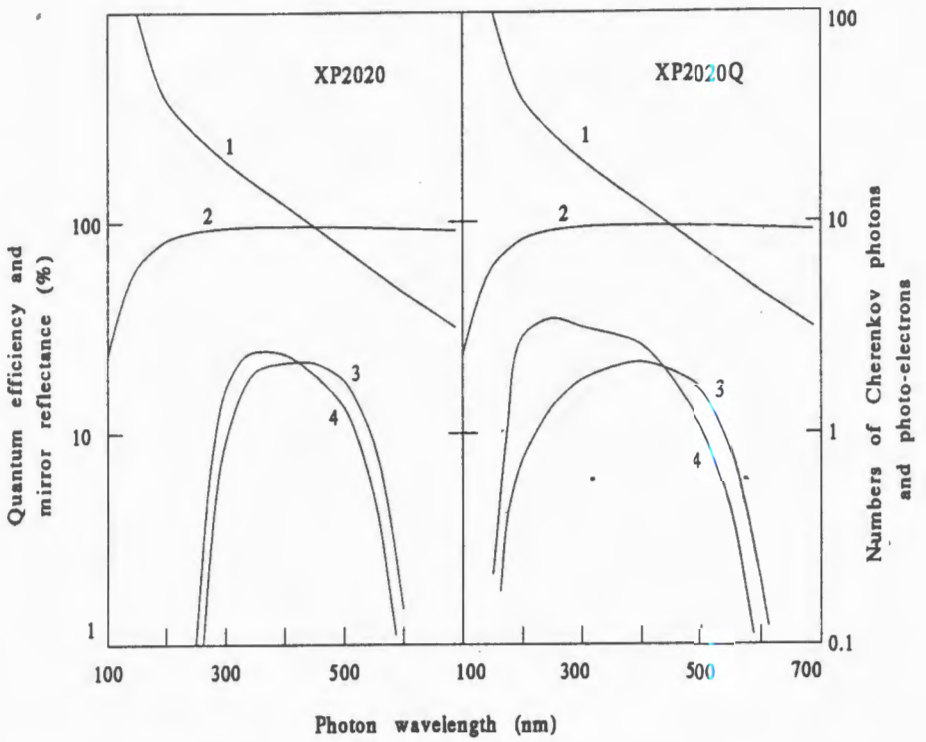

Fig.1. The mean number of photoelectrons versus photon wavelength (1 — number of Cherenkov photons, 2 — mirror reflectance, 3 — quantum efficiency of photocathode, 4 — number of photoelectrons)

Pb nucleus produces $\simeq 2700$ photons along 1 cm of air radiator in wave length interval $\lambda = 300 - 550$ nm and $\simeq 5700$ photons within interval $\lambda = 200 - 550$ nm corresponding to domain of maximum sensitivity of PMT XP2020 and XP2020Q, respectively, which have been used in BC. Figure 1 shows the mean number of photoelectrons versus photon wavelength, for these PMT.

In the case of Pb ion disintegration as a result of its collision with target or surrounding medium nucleus, response of the BC is proportional to the sum of charge squared of the projectile fragments if the distance between produced fragments is longer than the wavelength of Cherenkov radiation.

The layout of beam counters along the beam channel is shown in Fig.2. BC system of the CERES experiment consists of three Cherenkov detectors BC1, BC2, and BC3, and each of them solves its own functional tasks. To avoid upstream interactions as much as possible, a vacuum pipe is used up to the target region. The Cherenkov beam counter, BC1 has been installed in the beam pipe, 60 m upstream of the target. It is responsible for beam monitoring and start signal production by an incident ion. Detector BC2 is situated behind the CERES spectrometer, 6.35 m downstream of the target, and is responsible for detection

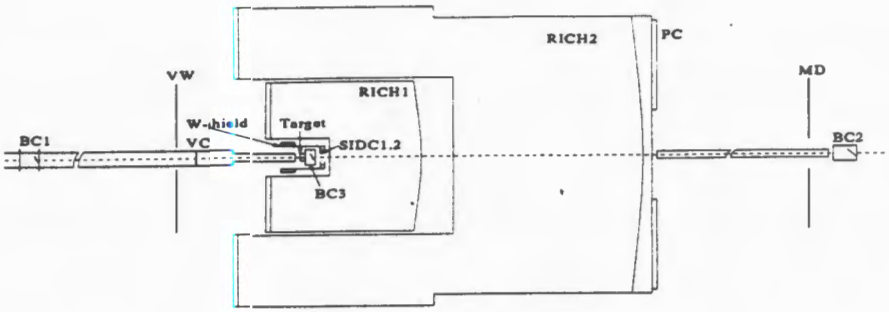

BC1, BC2, BC3 - Cherenkov Beam Counters *(Trigger detectors)*
VW - Veto Wall
VC - Veto Counter } *(Veto detectors of Trigger)*
SIDC1,2 - Silicon Drift Chambers
RICH1,2 - Ring Imaging Cherenkov detectors
PC - Pad Chamber } *(Main detectors of Spectrometer)*
MD - Multiplicity Detector *(Trigger detector)*

Fig.2. A layout of trigger detectors at the CERES experiment area

of projectiles passing through the experimental apparatus.The Cherenkov micro-counter BC3 is located right behind the target and its basic function is to establish a fact of nucleus-nucleus collision with the absence of Pb nucleus after the target. Interactions downstream of the target but in front of multiplicity detector (MD) cannot be ignored when triggering at low multiplicities. These events can be vetoed by BC3, too. The target is placed at the beam focus with the beam spot diameter of < 600 μm.

Good time characteristics of Cherenkov radiation and PMT XP2020 allow one to organize 10-ns coincidence of signals from BCs, for interaction trigger and also other additional triggers usefull for analysis of the beam passage and searching for background conditions.

Signals from BCs come to the fast discriminator (model 4F115 LHE, JINR) and Ch.ADC (LeCroy VME model 1182). Discrimination thresholds for BC1 and BC2, which have better amplitude resolution than BC3, are set down on the level of about 80% and for BC3 on the level of 50% of the mean pulse heigth of Pb nuclei. After fine adjustment of beam and counter operation we have the following condition for coincidence rates

$$BC1 \cdot BC2 = BC1 \cdot BC3 \cdot BC2$$

Interaction trigger was organized by means of coincidence of the logical signal from BC1 and veto signal from BC3.

So, with these three beam counters there were organized four different types of the simplest triggers:

1. beam trigger — BC1;
2. clear passage of beam ion without disintegration — $BC1 \cdot BC3 \cdot BC2$;
3. interaction trigger — $BC1 \cdot \overline{BC3}$;
4. background interaction behind the target — $BC1 \cdot BC3 \cdot \overline{BC2}$.

Logical signals from BC1, BC2, BC3 and interaction trigger are passed to the inputs of TDC (Le Croy VME model 1172) for off-line controle of the time structure of the signals and organization of B/A protection.

3. Beam Counters

The mirrors of the beam counters were done by vacuum evaporation of 0,999999 Al from the tantalum base on 12 μ mylar with very small heterogeneity over the thickness. The thickness of the settled aluminium layer was 500—800 Å. The factor of reflection measured for $\lambda = 200$ nm was 80%. Construction of Cherenkov counter BC1 is shown in Fig.3. There is no essential difference between the constructions of BC1 and BC2. Entrance window of BC2 was placed parallel with the mirror plane at an angle of 45° to the beam axis with the aim to minimize a path length scattering in radiator for different lead projectiles.

Geometry of the target region and construction of BC3 is shown in Fig.4. Cherenkov light produced in BC3 radiator by projectile is taken out with 2 m optical cable. Light-guide core of the cable has the diameter of 5 mm and consists of thin quartz fibre set with wavelength cut in ultra violet region at $\lambda_{min} = 180$ nm. One end of the cable enters to the radiator chamber of BC3 at angle of 45° and another one is connected with photocathode of PMT XP2020Q.

Before an installation of BC3 a fine tuning of the mirror position was done with special light source producing the light along the BC3 chamber axis. A method of the mirror adjustment was based on requirement to obtain light image around the centre of semi-transparent screen which was placed on the edge of an aluminium tube (entrance of the

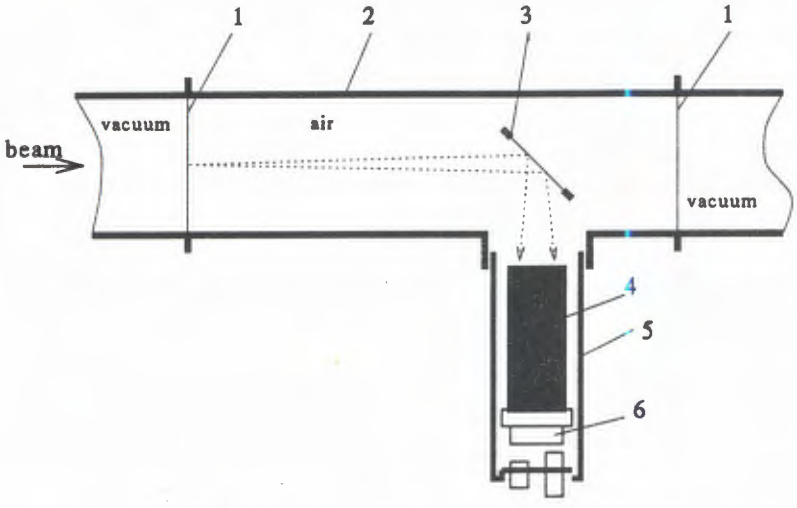

Fig.3. Construction of Cherenkov counter BC1 (1 — mylar windows, 2 —Cherenkov chamber walls, 3 — mirror, 4 — photomultiplier XP2020, 5 — soft iron tube, 6 — voltage divider)

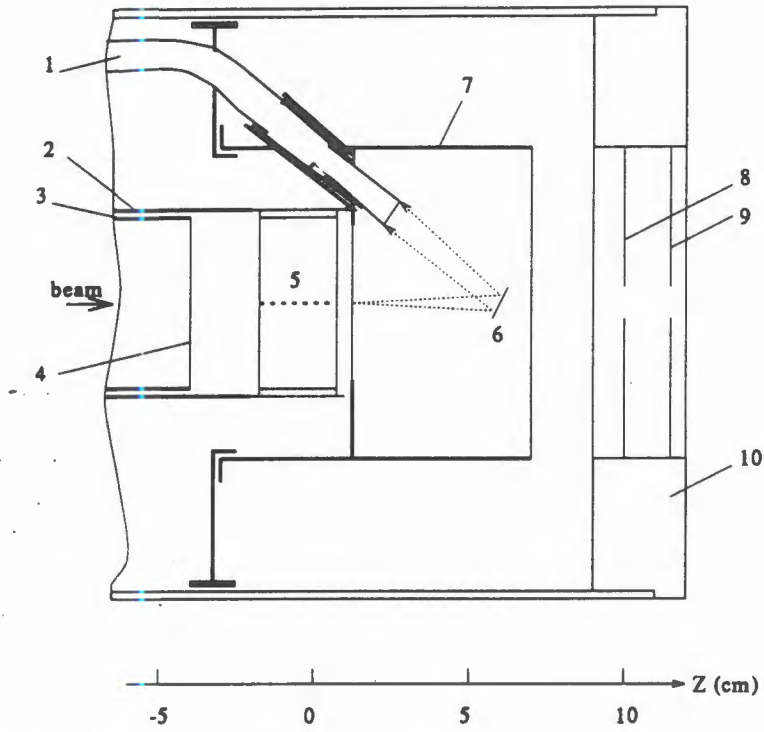

Fig.4. Target area and Cherenkov counter BC3 (1 — optical cable, 2 — carbon pipe, support of the target, 3 — vacuum carbon pipe, 4 — mylar window, 5 — target, 6 — mirror, 7 — Cherenkov chamber of the BC3, 8 — SIDC1, 9 — SIDC2, 10 — SIDC mechanical support)

optical cable into BC3 chamber). The geometry of BC3 was such that a lead nucleus passing through the radiator produces Cherenkov light spot on the polished edge of the optical cable with the lateral dimension less than the diameter of lightguide area. The basic characteristics of beam counters are given in Table 1 and list of constructive materials along the beam path is given in Table 2.

Special investigation has shown that light attenuation factor on the way mirror–optical cable–PMT is 7.5. It leads to the corresponding diminishing in the photoelectrons number on photocathode of PMT and as a consequence to the decreasing of the amplitude resolution relative to the values obtained with BC1 and BC2. The usage of optical cable and PMT with $\lambda_{min} \simeq 180$ nm in BC3 allows one to increase efficiency of Cherenkov radiation detection. Although, the length of radiator in BC3 chamber is rather short and light attenuation factor is rather high, there are $\langle N_e \rangle = 400 \pm 70$ photoelectrons from PMT photocathode created by Pb nucleus passing through the radiator.

Table 1

characteristics	BC1	BC2	BC3
air radiator length (mm)	170	206	43
beam spot			
x direction	±20 mm	< ±5 mm	< ±300 μ
y direction	±5 mm	< ±5 mm	< ±300 μ
mirror			
position from the target	60 m	6.56 m	59 mm
diameter (mm)	63	55	6
frame material	3 mm Al	3 mm Al	1.5 mm rohacel
angle to the beam axis	45°	45°	22.5°
PMT			
type	XP2020	XP2020	XP2020Q
λ range (nm)	300—550	300—550	200—550
rise time (ns)	1.5	1.5	1.5
pulse height resolution	7%	7%	7%
photocathode ⌀ (mm)	42	42	42

Table 2

Beam counter	Material	Thickness
BC1	mylar window 1	100 μ
	air	270 mm
	mylar mirror	17 μ
	mylar window 2	100 μ
BC2	black paper window 1	140 μ
	air	240 mm
	mylar mirror	17 μ
	black paper window 2	100 μ
BC3	black paper window 1	100 μ
	air	50 mm
	mylar mirror	13 μ
	black paper window 2	100 μ

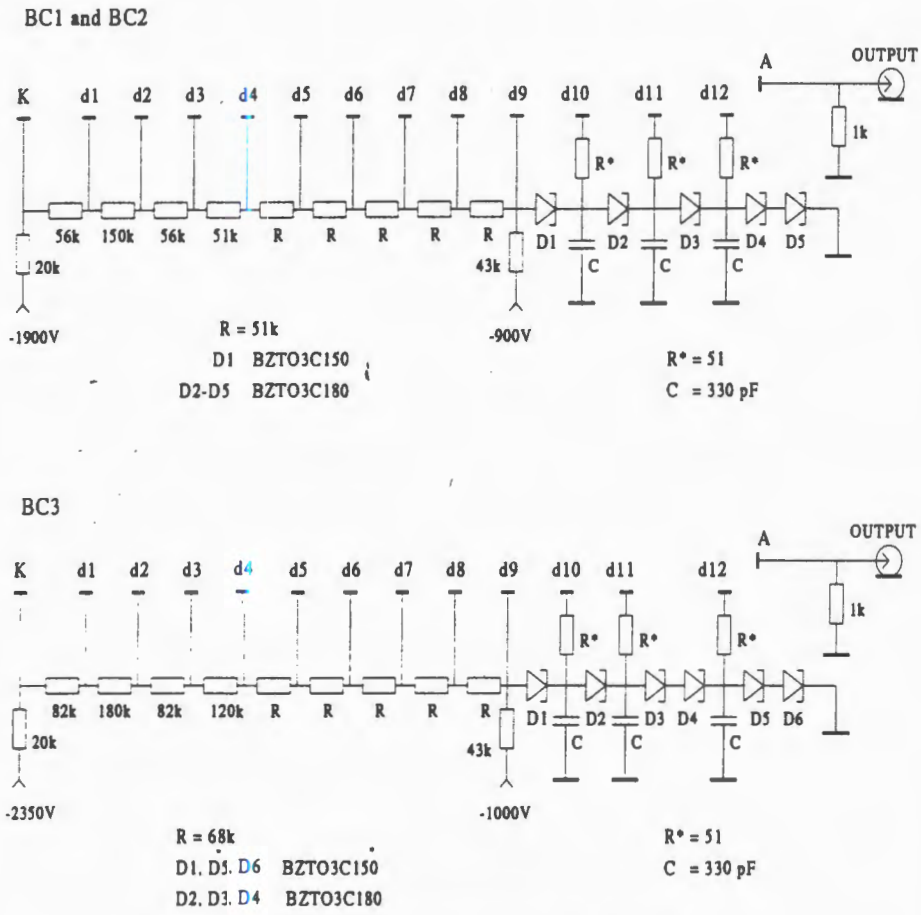

Fig.5. Voltage dividers of photomultipliers of the beam counters

To get a stable operation of PMT for high intensity of beam the voltage for last dynodes was created with a chain of diodes BZTO3C150, 180 and additional high voltage power supply. Scheme of the voltage divider is shown in Fig.5. Beam counters were supplied from the Le Croy high voltage multichannel system.

4. Beam Test

The first experience of the new BC system application in the level 1 trigger of the CERES experiment was performed with 160 GeV/n Pb beam in November/December 1995. The intensity of beam was about $5 \cdot 10^5$ ions/burst.

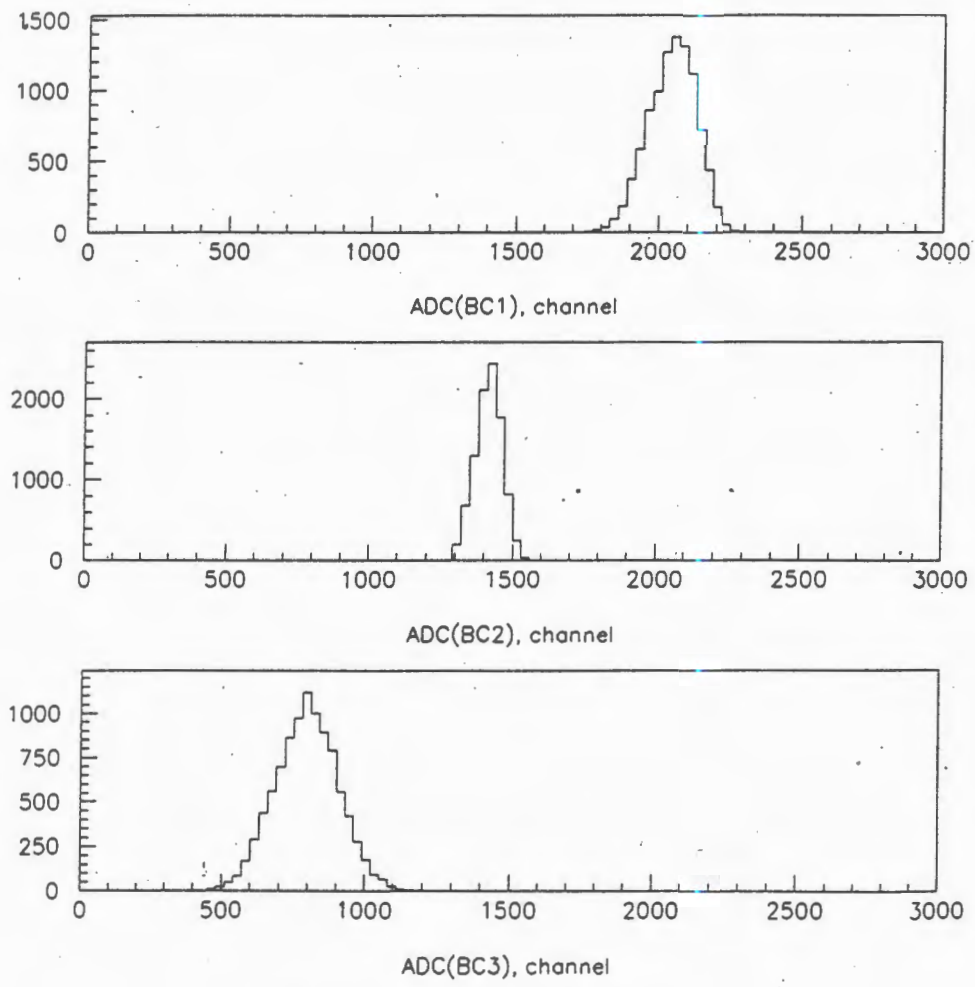

Fig.6. Responses of the beam counters for lead ions

4.1. Beam Counter Operation. An analysis of the operation characteristics of the counters showed the stable working capabilities of each beam counter during 25 days run. Study of the detector responses and the trigger operation during the run '95 was done with the special runs using the two simplest triggers: interaction trigger (trigger 3) and beam trigger (trigger 1). Taking into account the ADC and TDC information obtained with beam counters one can organize the additional triggers (2) and (4) mentioned above for the off-line analysis of clear passage of lead ions and background interactions. All beam counters had good responses for lead ions with the Gaussian shape of peak (relative uncertainty of ~4% for BC1 and BC2 and ~14% for BC3). The BC responses for lead ion obtained with trigger (2) are presented in Fig.6.

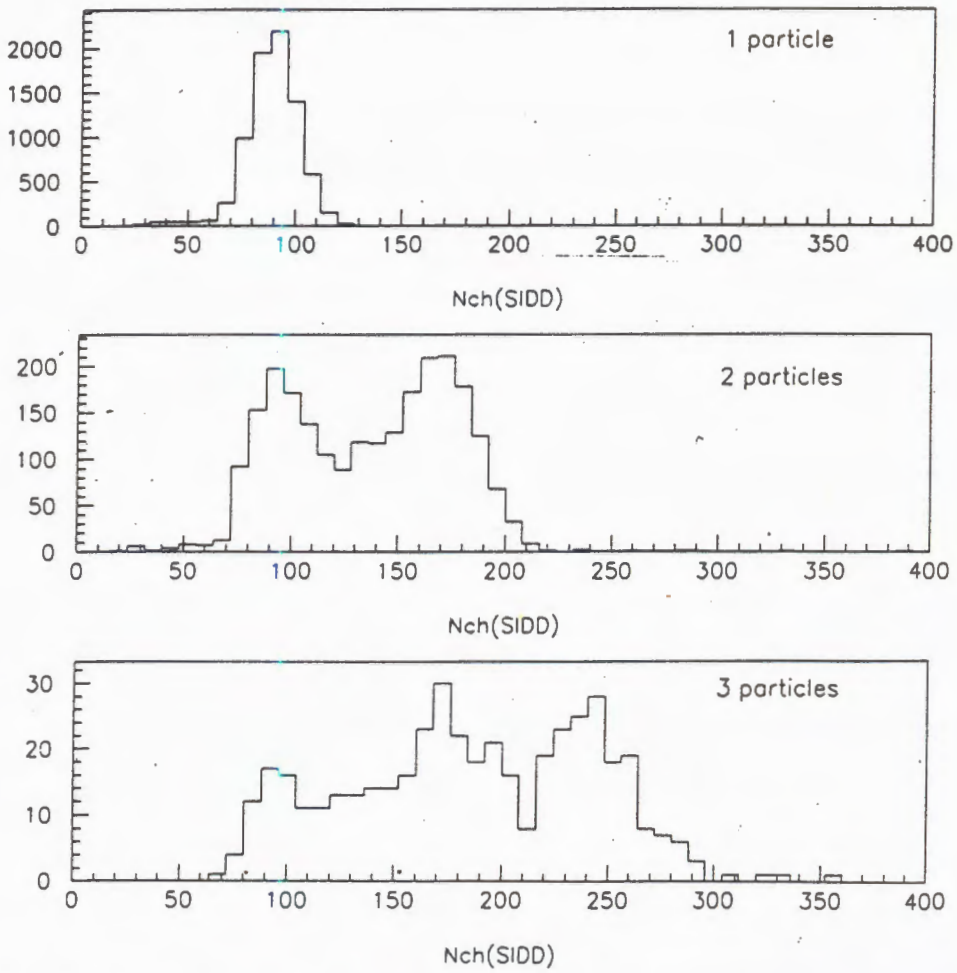

Fig.7. The response of the SIDC1 for one, two and three lead ions passing the target area without interaction within a time interval ± 5 μs

4.2. Before/after Protection. For the main detectors of the CERES spectrometer the background contribution to the detector response produced by pile-up of ions was analysed using the TDC information on a beam position on a time scaler obtained with beam counters. For this purpose trigger (2) was used for selection of the clear passage of lead ions through the experimental area. Under this condition, the background response of the SIDC is mainly produced by δ-electrons. Some additional number of hits appeared if more than one ion has passed through during the active time of the SIDC. The SIDC responses for three cases (1, 2 and 3 ions within the time interval ± 5 μs) are shown in Fig.7. The result is a rise of background with increasing a number of ions per active time of the detector. More clear information on the dependence of the number of background hits on

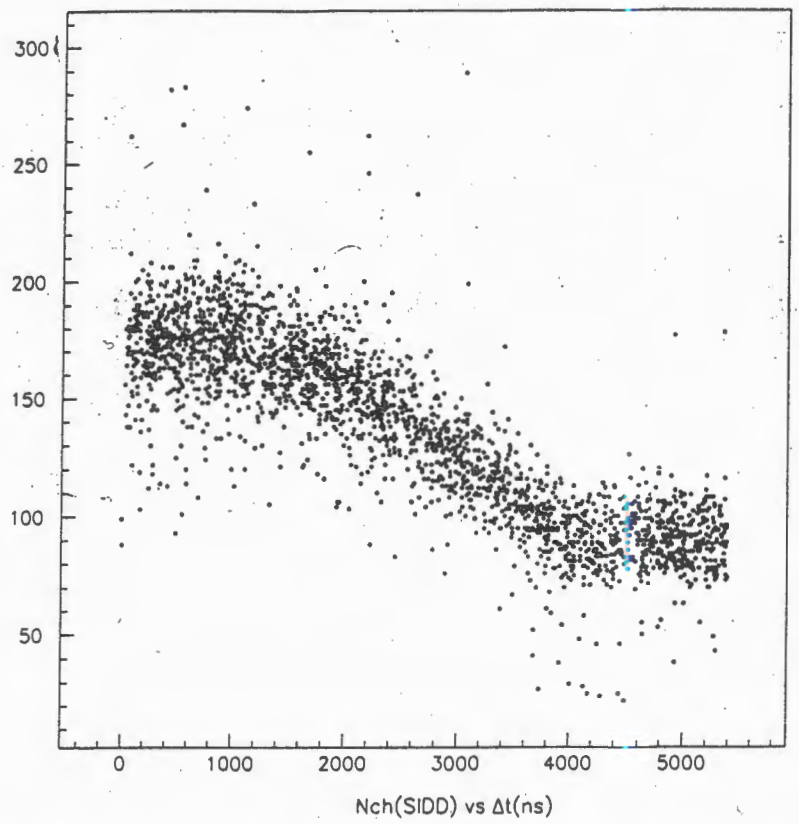

Fig.8. A background hit contribution to the SIDC1 response as a function of time interval between two lead ions passing the target area without interaction

the time distance between two ions is presented in Fig.8. One can see that the hits number increases from ~90 (one ion in the active time of the SIDC) to ~180 (two ions with a small time discrepancy) within the time interval ± 4 μs corresponding to the active time of the SIDC. This effect can be the main limitation in a way to work with a high intensity of beam.

4.3. Interaction Trigger. The major purpose of the interaction trigger for the CERES/NA45 experiment is an effective selection of Pb-Au collisions in the maximum wide region of impact parameter including closed and peripheral nuclear interactions. The main trigger function is to discriminate the BC3 signals with the pulse height more than threshold value settled as it has been mentioned above. The BC3 and BC2 responses are in a strong dependence on the lead ion fragmentation process and correspond to a sum of charges squared for fragments passing the radiator within the BC acceptance.

The Monte Carlo simulation of the perpendicular momentum distribution of lead ion fragments was estimated according to approach [2] with approximation of fragment charge composition [3]. The simulation results showed that the BC3 acceptance covers all

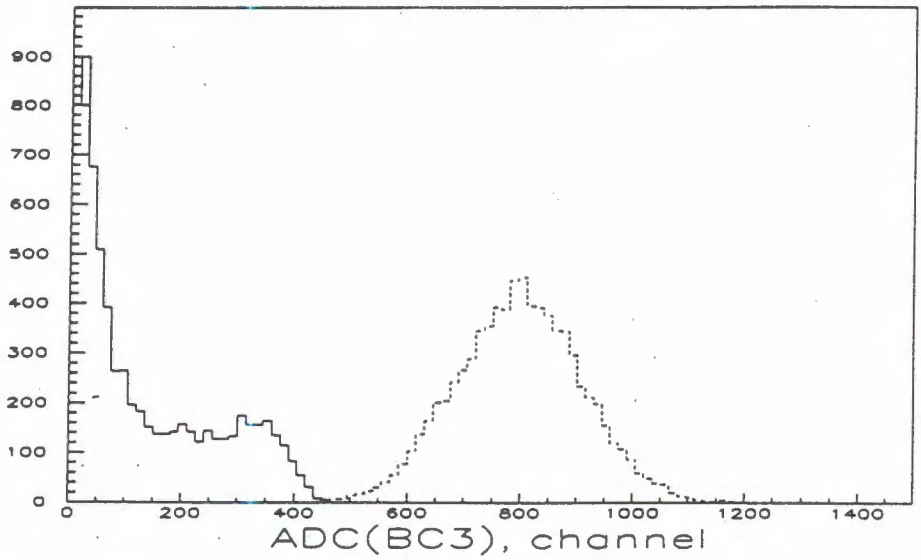

Fig.9. Pulse height distributions for Cherenkov counter BC3. Solid histogram — interaction trigger (3), dashed histogram — trigger (2)

projectile fragmentation region and the BC2 sees all fragments with charge more than 20, and some part of low charged fragments is missed.

The pulse height distributions obtained from the BC3 with two different triggers (2) and (3) are shown in Fig.9. The discrimination threshold was settled just before the peak produced by Pb and Pb-like-nuclei. A contribution of the different sources of lead ion disintegration, with a multiple production of charged particles in the target area selected by the interaction trigger, was studied by the vertex procedure where the interaction point was determined using the information from doublet of tracking devices SIDC1 and SIDC2.

The CERES target consisted of 8 disks with a thickness of 25 μm each and a diameter of 600 μm. They were spaced by 3 mm and a total thickness of target was 200 μm of Au. There were $\simeq 95\%$ of beam ions hitting the target. The largest amount of events concentrates in the target position ($-3 < z < 0$ cm) where all 8 microtargets are well seen separately as one can see in Fig.10. This figure demonstrates the MD response (charged particle multiplicity) versus z-coordinate of the vertex. The contributions from the interactions with mylar window of the vacuum pipe and the entrance window of the BC3 chamber are clearly visible at $z \simeq -5.3$ cm and 0.5 cm, respectively. For the further analysis of Pb-Au collisions we select only interactions with the target. In the frame of geometrical picture the geometrical cross section as a function of the impact parameter can be obtained by the integration over the overlaped region of the two nuclei. For Pb and Au nuclei the nuclear density is about constant and maximum up to radius $R \simeq 5$ fm and then the density falls down fast in a range $5 < R < 8$ fm with increasing of the radius. So the impact parameter $b < b_0 = 10$ fm corresponds to the interaction of two cores having the maximum density

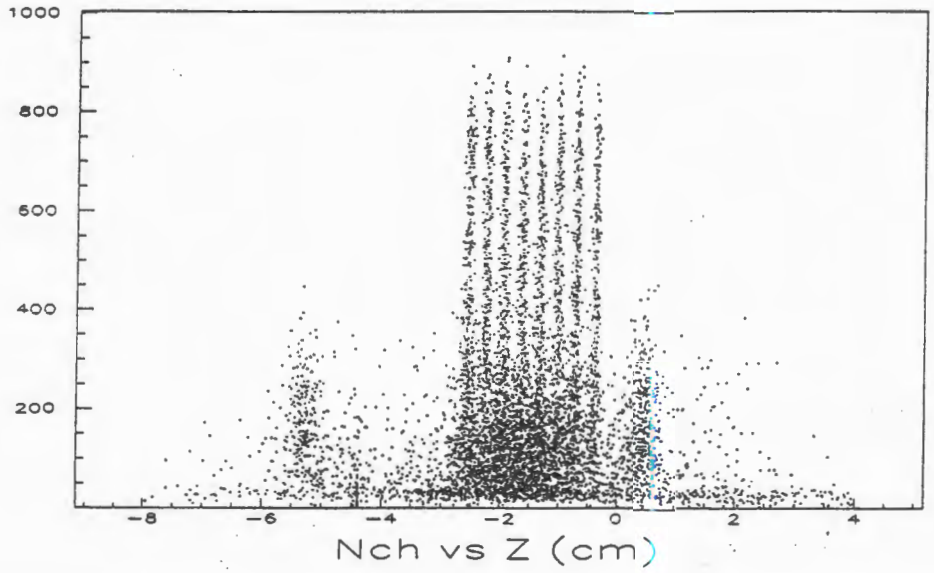

Fig.10. The sources of particle production in the target area presented as a correlation between MD response (number of charged particles, N_{ch}) and z-coordinate obtained by vertex

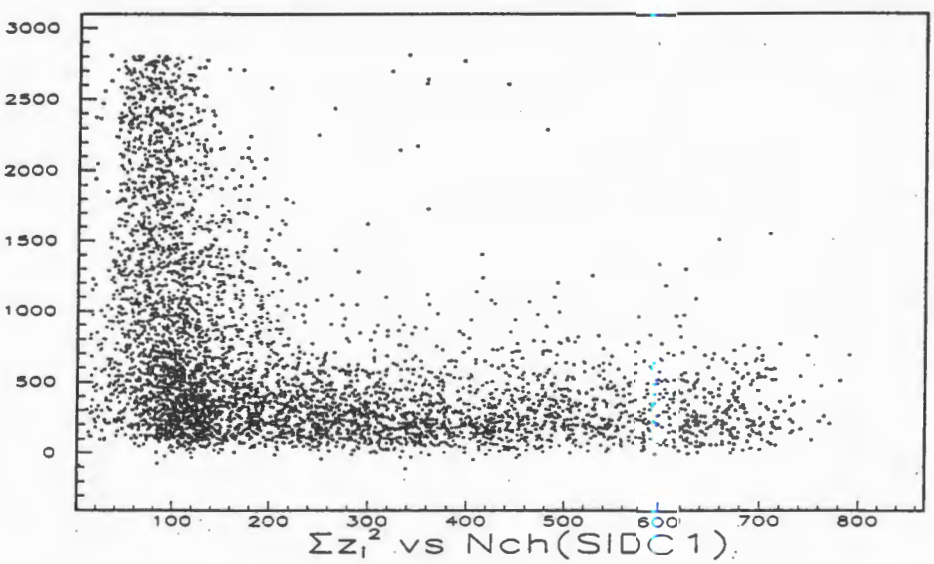

Fig.11. A correlation between the SIDC1 and BC2 responses measured for Pb-Au collisions with the interaction trigger

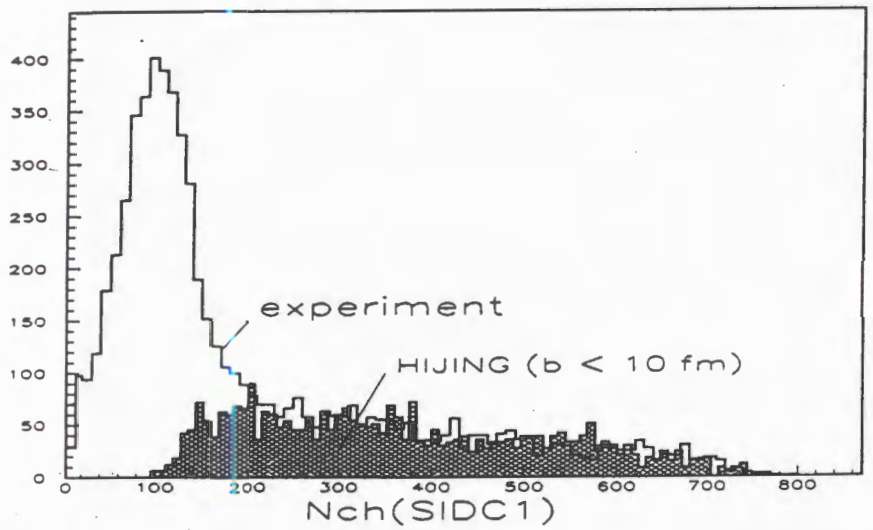

Fig.12. Multiplicity of charged particles produced in Pb-Au collisions within the SIDC acceptance measured with the interaction trigger and predicted by HIJING for $b < 10$ fm

which occurs in central and semicentral collisions. The geometrical cross section for these collisions can be calculated as

$$\sigma_c = \pi b_0^2 = 3.14 \text{ b}.$$

The radius range $5 < r < 8$ fm corresponds to a thickness of low density surface of Pb and Au nuclei and defines in the first approximation the geometrical cross section of Pb-Au peripheral collisions as

$$\sigma_p = \pi \cdot (b_{\max}^2 - b_0^2) = 4.90 \text{ b},$$

where $b_{\max} = 2 \cdot r_{\max} \simeq 16$ fm.

The experimental study of the trigger efficiency for closed and peripheral Pb-Au collisions was performed by analysis of a correlation between two processes, lead ion fragmentation (BC3 and BC2 responses) and the multiple production of charged hadrons in a midrapidity region corresponding to the maximum yield of secondaries and covered by the SIDC1 ($1.35 < \eta < 3.81$) and the MD ($2.94 < \eta < 4.70$). As an illustration the similar result on a correlation between the BC2 and the SIDC1 data is shown in Fig.11. The BC2 data were transferred to the scale of sum of fragment charges squared by a normalization

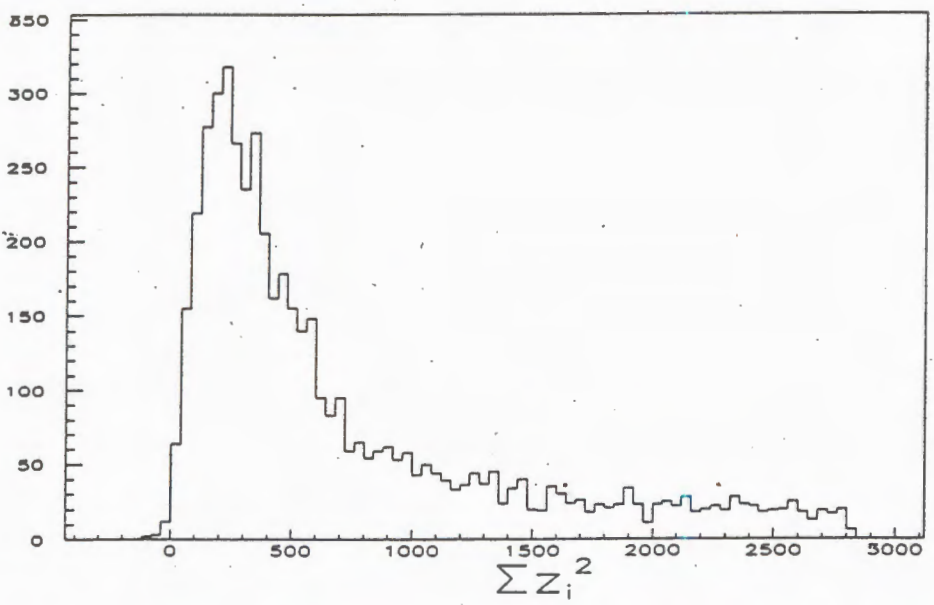

Fig.13. The distribution of sum of fragment charges squared measured for Pb-Au collisions with the interaction trigger

at Pb-ion peak position. The upper limit of the BC2 pulse height was reduced a bit with the aim to expel an influence of BC3 threshold. The large response of BC2 can be observed only for the SIDC multiplicities less than about 150. For the region of multiplicities more than 150, the interaction trigger selects all events without cut. A correspondence between the charged multiplicity within the SIDC1 acceptance and the impact parameter of Pb-Au collisions was investigated with the HIJING event generator [4]. A comparison of the HIJING model prediction for the collisions at $b < 10$ fm with the SIDC1 experimental data is shown in Fig.12. One can see that the HIJING reproduces well the experimental multiplicity data at $b < 10$ fm. The SIDC1 multiplicity of 150 is produced by the nucleus-nucleus collision at impact parameter $b_0 \simeq 10$ fm. The bump in the experimental data at low multiplicities $N_{ch} < 150$ corresponds to nucleus-nucleus collisions with $b > 10$ fm and has a clear and simple explanation taking into account a large geometrical cross section of peripheral collisions.

So the interaction trigger works with the efficiency of $\simeq 100\%$ for semicentral and central collisions. The big dispersion of the Σz_i^2 value in the low multiplicity region due to the event-by-event fluctuation of Pb-ion disintegration in the peripheral collisions is observed and there is a high probability of strong disintegration of Pb nuclei without any high-charged fragments even in the peripheral collisions.

Table 3

Impact parameter region	Z_{max}
$b < 8$ fm	< 25—30
$b < 10$ fm	< 40—$50 \simeq 0.5Z_{Pb}$
$b > 10$ fm	$< 0.5Z_{Pb}$, for the most fraction of events

The upper limits of fragment charge, Z_{max}, for different impact parameter regions estimated on the experimental results are given in Table 3. The pulse height distribution measured by the BC2 with the interaction trigger is presented in Fig.13. The measurements showed that the threshold of the trigger cuts only a small fraction of the nuclear inelastic peripheral collisions. The cross section of peripheral collisions registered can be estimated as

$$\sigma_p^{exp} = \sigma_c \cdot \frac{N_p}{N_c} = 4.35 \text{ b},$$

where N_p and N_c are number of events with N_{ch} (SIDC1) < 150 and > 150, respectively. This experimental value is only a bit less than one obtained above in a frame of geometrical

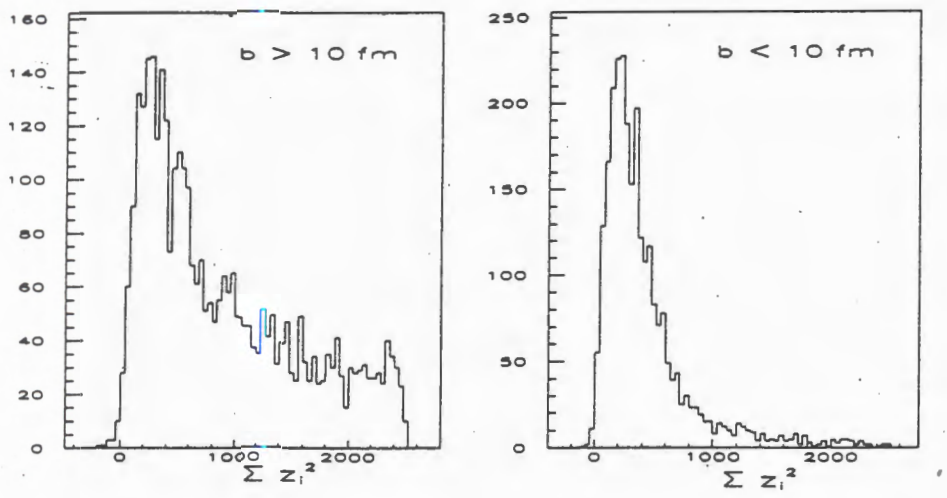

Fig.14. Experimental distributions of a sum of charges squared of lead fragments (BC2 data) for Pb-Au collisions for two impact parameter regions, $b > 10$ fm (left) and $b < 10$ fm (right)

picture of collision. The Σz_i^2 experimental distributions obtained with the BC2 for two cases of Pb-Au collisions with impact parameters $b > 10$ fm ($N_{ch}(\text{SIDC1}) < 150$) and $b < 10$ fm ($N_{ch}(\text{SIDC1}) > 150$) are shown in Fig.14. Here one can see separately the fragmentation of Pb ions in closed and peripheral collisions with Au-nuclei at 160 GeV/n energy and that there are no high-charged fragments at semicentral and central collisions.

We suppose that presented results can be of interest for the trigger design for the central and peripheral nucleus-nucleus collisions study as well as for testing of theoretical models including the description of the projectile nucleus fragmentation at ultrarelativistic energies.

5. Conclusion

The system of Cherenkov gaseous beam counters for monitoring of ultrarelativistic lead ions and an interaction trigger design was developed for the CERES/NA45 experiment in CERN. Test measurements with the lead beam at 160 GeV/n showed that such devices are capable to operate for a long term without any changes of their characteristics. The installation of the beam counters on a beam line led to a very small rise of the background. The analysis of detector responses showed the 100% efficiency of the interaction trigger for semi-central and central collisions of Pb and Au nuclei with low contribution of background interactions with window foils of vacuum pipe and Cherenkov counter chamber, BC3. We intend to continue our work on a development of the beam counter system for the CERES experiment and believe it has a good outlook.

6. Acknowledgements

We would like to thank the members of the CERES collaboration for their help in detector integration into spectrometer scheme. Specially we wish to acknowledge Profs. I.Tserruya, P.Glassel, and P.Wurm for their support of our work and the stimulating discussions.

References

1. CERES/NA45 Report to Cogne 1995, CERN/SPSLC 95-20, 1995.
2. Lepore J.V., Riddel D.J. — Report LBL-3086, 1974.

3. Adamovich M. et al. — Zeitsch. Phys., 1992, v.C55, p.235; Krasnov S.A. et al. — JINR Communications, P1-88-252, Dubna, 1988.
4. Wang X.N., Gyulassy M. — Phys. Rev., 1991, v.D44, p.3501; Phys. Rev., 1992, v.D45, p.844.

Received on December 10, 1996.

УДК 539.1, 0.74.2;
57-72: 539.12

A PROFILE-BASED GASEOUS DETECTOR WITH CAPACITIVE PAD READOUT AS THE PROTOTYPE OF THE SHOWER MAXIMUM DETECTOR FOR THE END-CAP ELECTROMAGNETIC CALORIMETER FOR THE STAR EXPERIMENT

G.Averichev, S.Chernenko, E.Matyushevsky, A.Nikiforov, Yu.Panebrattsev, E.Platner*, E.Potrebenikova, D.Razin, S.Razin, L.Smykov, G.Škoro, A.Shabunov, I.Tsvetkov, V.Yurevich, Yu.Zanevskiy

The results of testing the full-scale prototype of a profile-based shower maximum detector with external pick-up pads for the end-cap electromagnetic calorimeter (EMC) for the STAR experiment at RHIC are presented. It is shown that the plastic streamer tubes with coverless profile operating in proportional mode with low gain are suitable basic unit for shower maximum detector.

The investigation has been performed at the Laboratory of High Energies, JINR.

Газовый детектор на основе профиля с емкостным pad-считыванием как прототип детектора максимума ливня для торцевого электромагнитного калориметра эксперимента STAR

Г.Аверичев и др.

Представлены результаты испытаний полномасштабного прототипа детектора максимума ливня на основе пластикового профиля с емкостным pad-считыванием для торцевого электромагнитного калориметра STAR эксперимента на RHIC. Показано, что пластиковые стримерные трубки с открытым профилем, работающие в пропорциональном режиме с низким усилением, являются подходящим базисом для детектора максимума ливня.

Работа выполнена в Лаборатории высоких энергий ОИЯИ.

1. Introduction

In our previous report [1] we presented the results of Monte Carlo (MC) simulations and conceptual design of gaseous Shower Maximum Detector (SMD) with pad (strip) readout of signal for end-cap EMC of STAR experiment at RHIC [2]. Two types of detectors were proposed: MWPC and profile-based chamber. A possibility of using plastic streamer tubes operating in proportional mode with analog readout of external pick-up pads

*Rice University, Bonner Nuclear Laboratory, Houston, TX77251, USA.

(strips) for precise coordinate measurements is attractive for us. Profile-based particle detector can be as precise as conventional MWPC with pad (strip) readout [3], [4]. Detector mechanical tolerances are significantly relaxed. The space resolution would be determined by the quality of pad (strip) board and readout electronics.

The shower maximum detector will be placed in thin 25 mm gap in the end-cap EMC. The number of γ's in the SMD acceptance is about 800 for the central Au-Au collision at RHIC energies and the number of charged particles is the same. The showers as well as charged particles will be detected. The size of pads decreases going towards the beam axes to resolve ambiguities due to increasing multiplicity. The time between bunches at RHIC will be about 100 ns. So for high time occupancy a readout electronics need have an integration time about 50 ns, wide dynamic range, small signal/noise ratio for various pad's capacitance and as small as possible power dissipation.

Following the above arguments and reasoning our report [1] we have manufactured a full scale profile-based shower maximum detector prototype with pad capacitive readout. In this report we present results of testing the prototype with a certain suitable readout electronics.

2. Description of Prototype

A schematic view of the cross section of the prototype and the layout of measurement is shown in Fig.1. The prototype consists of four plastic profile tubes each with 8 cells of 9×9 mm^2 in size with 1 mm thick separating walls inserted in a gas-tight plastic envelope. The profile used for the prototype was one of those made for the DELPHI hadron calorimeter [5]. The inner cathode surface of profile is coated with resistive carbon paint. The cathode resistivity of the profile is about $200K\Omega$ per square. The anode is the gold plated tungsten wire of 20 μm diameter strung in each profile cell with tension of 80 g and

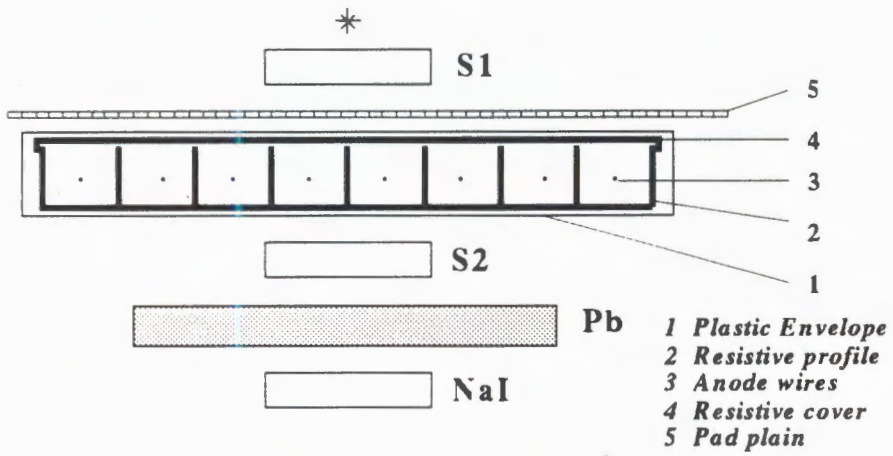

Fig.1. Block diagram of the test set-up

supported by spacer in the middle point. The gas mixture used is argon + isobutane in the ratio 4:1 at normal pressure.

The size of the prototype is 40×120 cm^2. Both tubes with resistive cover and coverless have been used in prototype tests.

The G10 outer pad (strip) board with pads (strips) facing detector is placed directly on the tube plastic envelope. The sizes of the pads are 4×40 mm, 12×130 mm and 12×400 mm. Readout electronics is placed on the opposite pad side of the board.

The anode wires in each tube are connected together serving one readout channel. The anode signals are used only for tuning of operational high voltage applied to the tube.

3. Front End Electronics

Following the results of MC simulation the total electronic channel number of the end-cap EMC shower maximum detector should be about 25000 with analog readout of anode wires (2000 channels) and cathode pads (23000 channels). The position of shower or the entrance point of minimum ionizing particle (MIP) will be measured. Front End Electronics (FEE) is needed for a fast two-dimensional coding of the analog data.

The spatial resolution achievable by using an interpolation method depends on several parameters, in particular on the signal-to-noise ratio S/N. A small noise allows one to reach wide dynamic range at lower gas gain and, consequently, to slow down the detector aging.

The major problem of the FEE design is an extremely limited space (25 mm) given for placing the shower maximum detector with the associated electronics and the cable communications that imposes the request of as small as possible power consumption [2].

Therefore the main parameters of the FEE are: peaking time (T_p), dynamic range, S/N and power dissipation per channel (P_D).

Peaking time T_p should be matched to one half of the crossing time (the time between bunches). At high channel occupancy (up to 100% for Au-Au collisions) the drift time should not exceed the value of the crossing time, i.e., 100 ns. For the typical drift velocity of about 20 (ns/mm)$^{-1}$ this means that in the final design the profile cell size must be about 5-6 mm.

Mean number of particles in shower is about 100, so a noticeable total charge will be collected even at such small peaking time. But for MIP we should increase the gas gain.

To meet the high count rate (T_p ~50 ns) and the low noise ($< 2000e^- \alpha C_{pad}$ ~ hundreds pF) a bipolar IC technology is more preferred instead of CMOS. A common emitter chain in the first stage of the preamplifire (PA) with resistive feedback, forming a transimpedance amplifier, can provide the high gain at acceptable power. To prevent strong the gain and a pulse shape degradation at a large input capacitance, the PA should have a high value of open loop gain [6]:

$$V_{out} \sim \frac{Q_{in}}{C_f^{eff}}; \quad \tau_{rise} \sim \frac{C_{pad} C_c}{g_m C_f^{eff}},$$

where $C_f^{eff} = C_f + \frac{C_{pad}}{g_m R_c}$ — effective feedback capacitance, R_c, C_c — collector resistor and capacitance, respectively, and g_m — transconductance of a bipolar transistor.

If open loop gain $g_m R_c$ is rather large, the sensitivity of PA to C_{pad} value is reduced. However it demands higher $g_m \sim I_c$, i.e., to increase power consumption. Also serial noise must be small at short T_p.

To keep good double pulse resolution and high value of S/N ratio, the PA has to be followed by a multipole shaping amplifier (SA). The shaper should include also $1/t$ tail cancellation and transform input pulse into a near Gaussian shape. From EMC physics considerations the dynamic range is requested as large as 1000. This value is more than enough for getting needed spatial resolution in interpolation method (~ 0.1 of pad pitch) [7]. Concerning the FEE design it is desirable to realize this parameters at low, as possible, noise and, hence, smaller power dissipation.

After amplifying and shaping, the data from SMD have to be delayed and digitized. Since SMD is a fast detector, the readout electronics delay circuits have to provide write and readout modes simultaneously. The delay of ~ 1 μs, needed for level 0 trigger decision, can be performed, in principal, by two ways as shown in Fig.2.

First (Fig.2a), analog is based on Sequential Capacitors Array (SCA) and second (Fig.2b), the flash ADC with digital pipeline is used. The solution based on SCA approach is cheaper and consumes significantly lower power. The suitable number of pipeline cells is 10 + 20. Application of higher clock frequency (up to 40 MHz) can give a possibility to know a channel history and make an amplitude correction. The number of the ADC bits

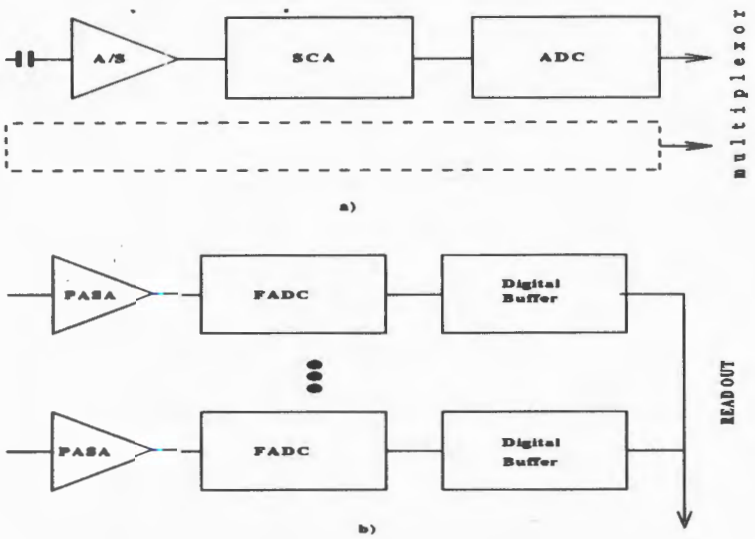

Fig.2. The scheme of different variants of shaped SMD signal delay

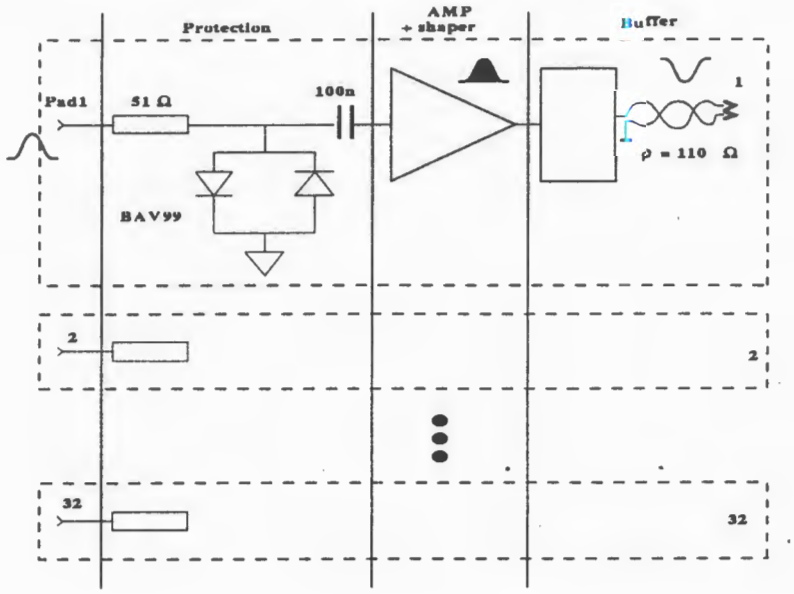

Fig.3. The scheme of readout electronics based on 32-channel chip for the SMD prototype test

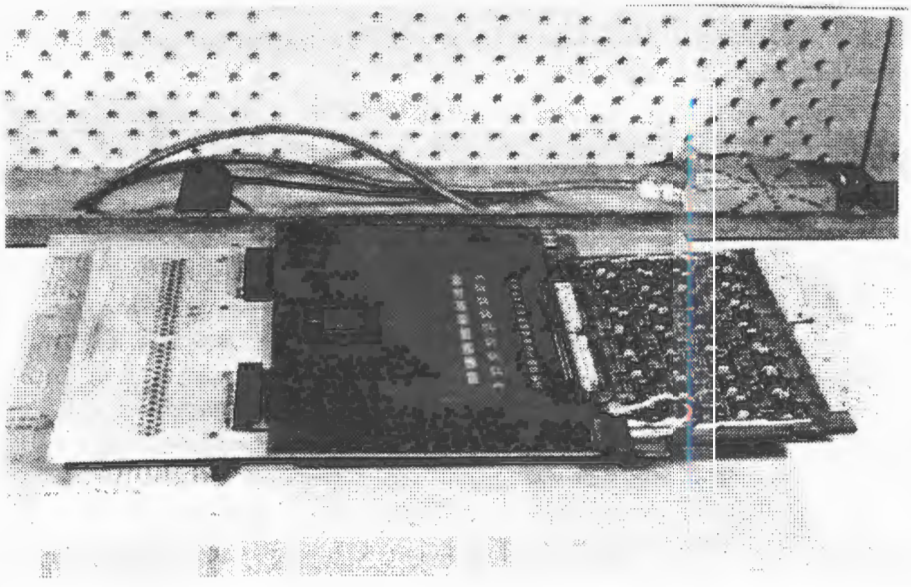

Fig.4. View of the shower maximum detector prototype

must be matched to dynamic range. Therefore FEE should use 10-bits linear or 8-bits non-linear ADC.

Following the arguments described above we have designed the multichannel electronics based on 32-chip (PASA) [8] developed by D.Dorfan (US, Santa Cruz) for testing the SMD prototype. This IC has extremely low power consumption ~ $2mW/ch$. Other parameters such as peaking time ~ 75 ns, $1/t$ cancellation and low noise (5 nA, r.m.s) are near needed for the prototype.

Our goals were:

1) to design electronics for prototype test with a radioactive source and a beam,

2) to investigate possibilities of a low power consuming chain implementation for readout of signals from large pads.

The arranged scheme of protection diodes at inputs and drivers at outputs to route data on cable is shown in Fig.3. The output pulses are transferred via 5 m long TWP flat cable to 9-bit ADCs.

Figure 4 shows a general view of the shower maximum detector prototype on the side of the pad board. The 32-channel PASA chip has been mounted on individual board. The connection with pads was realized via input protection circuits by means of 32-pins connectors. Various type pads can be connected by turns to the chip inputs.

4. Test Studies of Prototype Performances

Two types of plastic tubes were used in test studies: with profile closed by resistive cover and with coverless profile. The measurements were carried out using electrons (the energy up to 3 MeV) from ^{144}Ce radioactive source. The unnecessary substance from upper and lower prototype screening boards were removed. The narrow upper collimator (2 mm diameter slit) was used to define a narrow beam over pad.

The electrons with the energy more than 2 MeV are passed through scintillation counters S1—S2 (energy loss ~ 1 MeV) and a plastic tube (energy loss ~ 1 MeV). Signals from scintillation counters (S1 and S2 in Fig.1) form the trigger for the ADC gate.

In experiments with cosmic muons additional large NaI counter was used for the ADC gate trigger, too.

Figure 5a shows the amplitude spectra of an individual pad (4×40 mm) at various operating voltage. The pedestal peak is well separated from the minimum ionizing signal.

Measurements data with cosmic muons for six nearby pads at 1725 V operational voltage in Fig.5b shows the same (the ADC's pedestals were subtracted).

The data for middle 12×130 mm and large 12×400 mm pads are shown in Fig.6.

It is seen that at operating voltage value of about 1700 + 1750 V we have well defined signal from minimum ionizing particle. The tube operates in the proportional regime with the gain at the level of 10^4—10^5. The pulse duration does not exceed ~ 150 ns at 1/10th of maximum height for different input pad capacitances of readout electronics. The output signal amplitude is nearly proportional to the value of pad capacitance that means the preamplifier gain doesn't change noteceably.

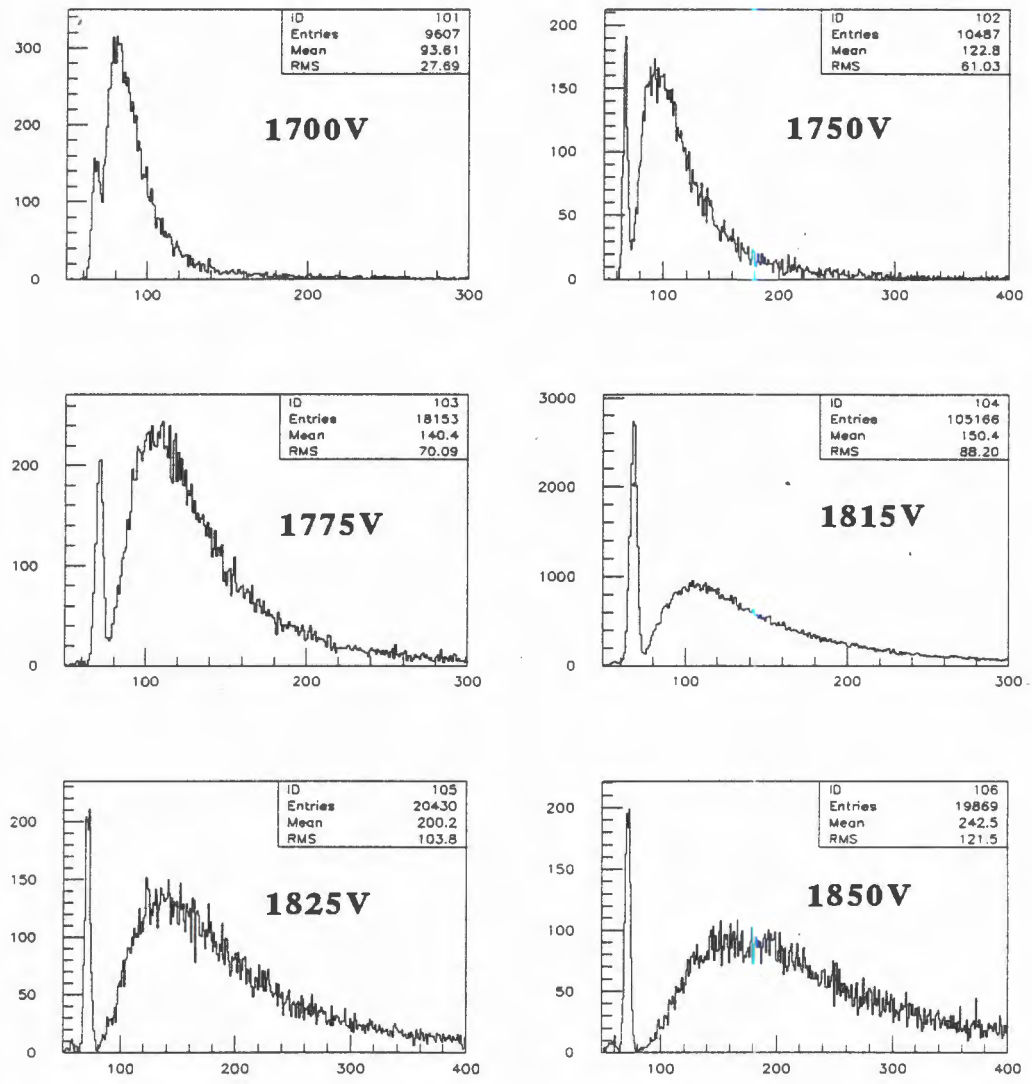

Fig.5a. The amplitude spectra of individual 4×40 mm pad at various operation voltage. Measurements with radioactive source ^{44}Ce

The amplitude spectra for a tube with coverless profile for four nearby 4×40 mm pads is shown in Fig.7.

To investigate the position resolution we have measured a distribution of charge induced on the six nearby pads. The measurements with the tubes with profile closed by resistive cover have been made using cosmic muons. In experiments with the tubes with coverless profile the collimated radioactive source was used. The events with maximum charge on the middle (third) pad were selected.

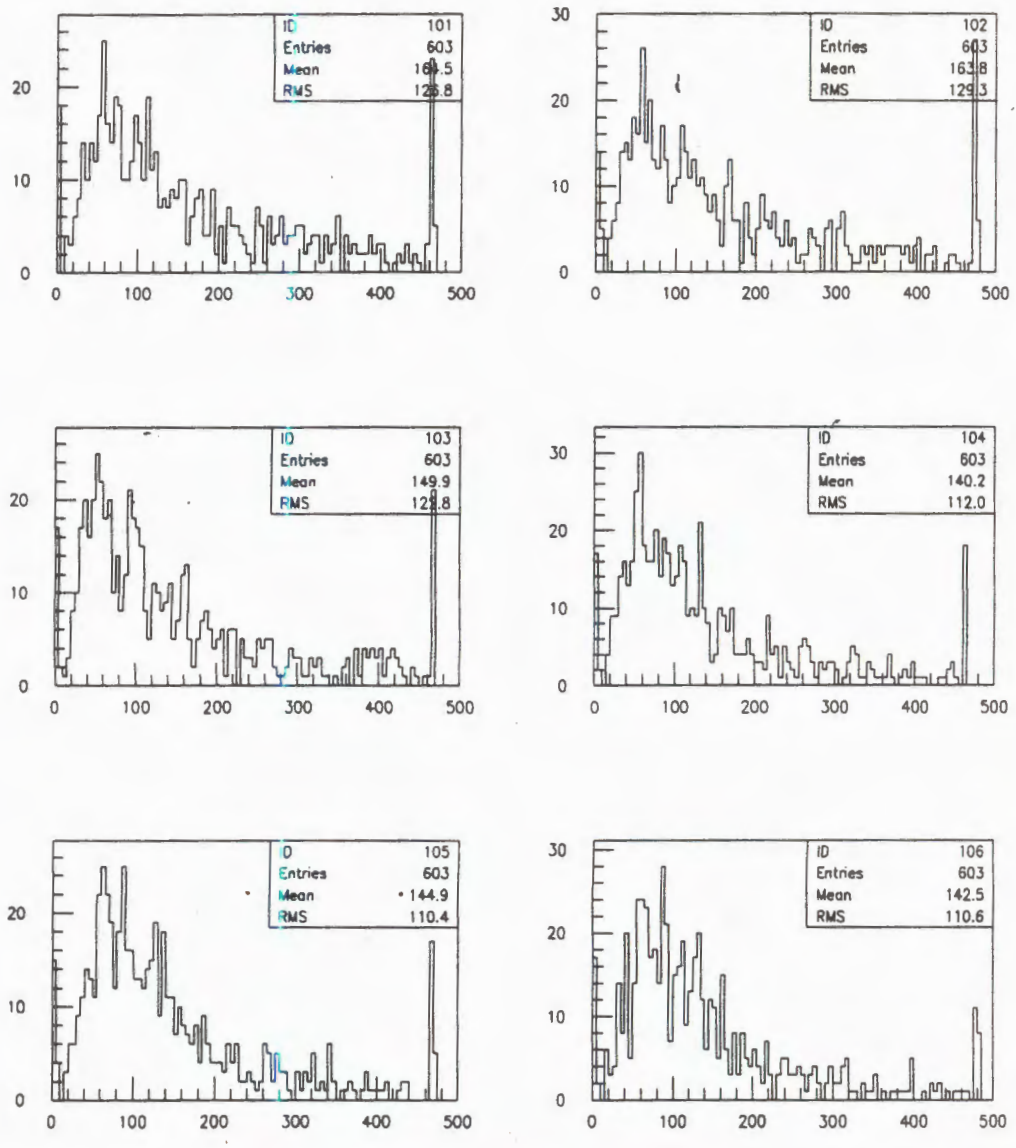

Fig.5b. The same as Fig.5a at 1725 V operation voltage. Measurements with cosmic muons for six nearby pads

In Fig.8 the distributions of charge over six 4×40 mm nearby pads for a tube with coverless profile and for a tube with profile closed by the resistive cover are shown.

It is seen that the distribution for the tube with coverless profile is narrow enough so it will be possible to separate particles in high multiplicity collisions.

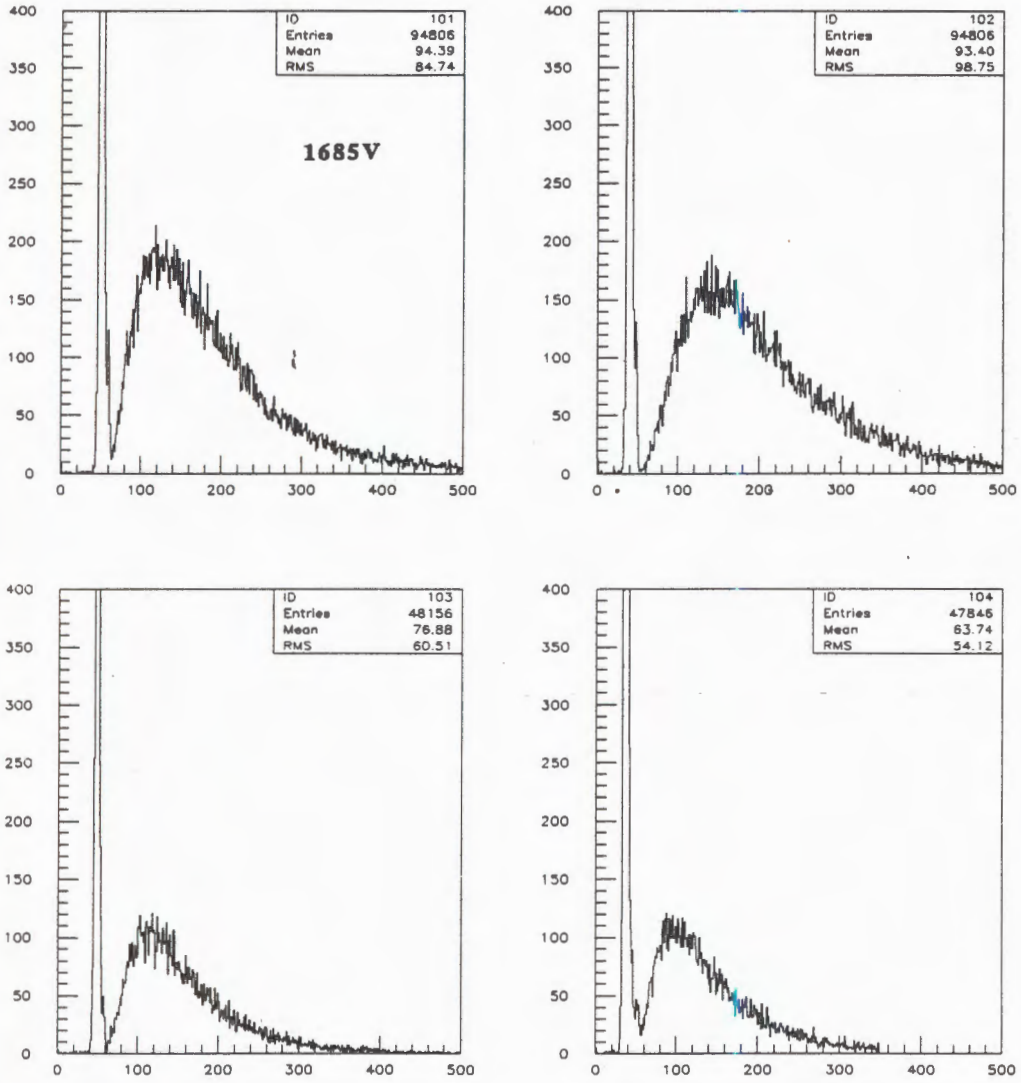

Fig.6. The amplitude spectra for two nearby 12×130 mm (top) and 12×400 mm (bottom) pads. Attenuation is 5 (top) and 10 (bottom)

In Ref.9 the detector of electromagnetic shower on the basis of plastic streamer tubes has been investigated but there the tubes operated in high saturated mode with worse spatial resolution and lower rate capability.

The spatial resolution of detectors on the base of plastic streamer tubes with capacitive readout has been investigated in [3,4,10]. It was found that nonuniformity of cathode resistivity significantly impairs the spatial resolution and to use the tube with very high cathode resistivity ($> 10M\Omega$) or with low resistivity and coverless profile is preferable.

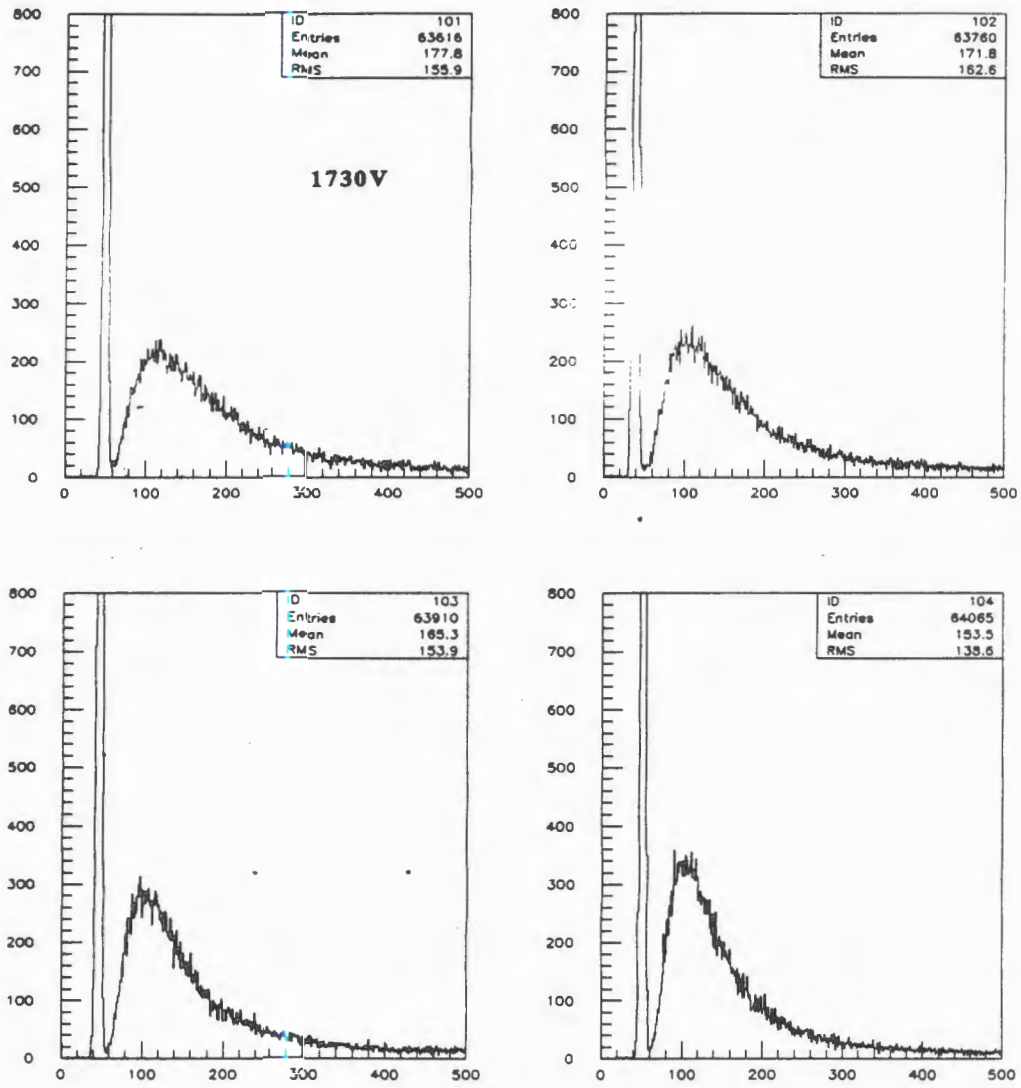

Fig.7. The amplitude spectra for 4 × 40 mm four nearby pads for a tube with open profile

5. Conclusion

The test investigations of the prototype based on the plastic streamer tubes show that the coverless tubes with capacitive readout operating in proportional mode with low gain are suitable basic unit for the end-cap EMC shower maximum detector. The uniformity of

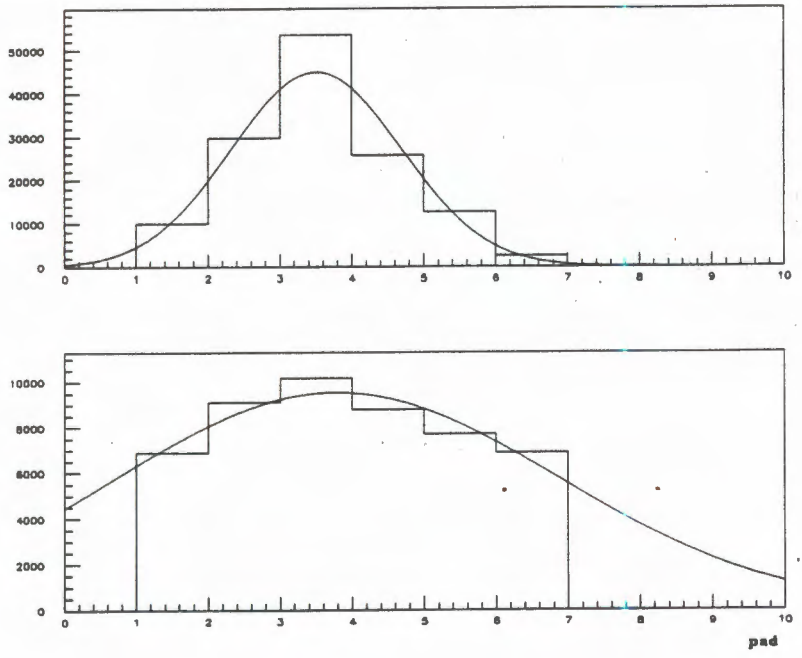

Fig.8. Charge distribution on six nearby 40 × 40 mm pads for a tube with opened (top) and closed (bottom) profile

the cathode resistivity has a major influence for spatial resolution. The tubes with coverless profile and low resistivity are more preferable.

The readout electronics based on the 32-channel chip PASA [8] can be used for the detector with the 9×9 mm^2 cell plastic tubes.

Acknowledgements

The authors would like to thank R.Baur, S.Heppelmann, S.Kleine, D.Underwood, A.Olshevskiy, G.Alexeev, A.Sadovsky for their help in this investigation and useful discussions.

The authors are grateful for support by the Russian Fundamental Science Foundation under grant 95-02-05061 and the RHIC Department at BNL under contract 776746.

References

1. Averichev G. et al. — JINR Rapid Communications, 1996, No.6[74]-95, p.95-108.
2. The Electromagnetic Calorimeter for the Solenoidal Tracker at RHIC. A Conceptual Design Report, Pub-5380 (1993).

3. Khovansky N. et al. — Nucl. Instr. and Meth., 1994, v.A351, p.317.
4. Bonushkin Yu. et al. — Nucl. Instr. and Meth., 1991, v.A300, p.268.
5. The DELPHI Technical Proposal, CERN/LEPS/83-66/1 (1983); DELPHI collaboration (P.Aarnoi et al.); Nucl. Instr. and Meth., 1991, v.A303, p.233.
6. Newcomer F.M. et al. — IEEE Tr. on Nucl. Sci., 1993, v.40, No.4, p.630.
7. O'Connor P. — Proceedings of the International Conference on Electronics for Future Colliders. New York, May 4-5, 1993, p.16.
8. Platner E., Theman H. — STAR Note 173, April 1994.
9. Belousov V.I. et al. — STAR Note 184.
10. Korytov A. et al. — Nucl. Instr. and Meth., 1994, v.A338, p.375.

Received on December 12, 1996.

УДК 539.122

WHAT DELPHI CAN GET WITH AN UPGRADED POSITION FOR THE VERY SMALL ANGLE TAGGER

S.Almehed[1], *G.Jarlskog*[1], *F.Kapusta*[2], *U.Mjornmark*[1], *I.A.Tyapkin*[3], *N.I.Zimin*[3]

A rather large profit can be obtained for two-photon physics studies with an upgrade of the DELPHI very small angle tagger position. Results have been obtained by using FASTSIM simulation both for double tagged and single tagged modes of $\gamma\gamma$ interactions, and for Bhabha events used for the luminosity measurements.

The investigation has been performed at the Laboratory of High Energies, JINR.

Что ДЕЛФИ может выиграть при изменении положения детектора мечения под очень малыми углами

С.Алмехед и др.

Довольно большой выигрыш может быть получен при изменении положения детектора мечения под очень малыми углами установки ДЕЛФИ. Приведенные результаты были получены с помощью программы моделирования FASTSIM для двухфотонных взаимодействий с одним и двумя мечеными электронами и для процесса рассеяния Баба, используемого для измерения светимости.

Работа выполнена в Лаборатории высоких энергий ОИЯИ.

1. Introduction

It was mentioned in the recently published report of the Workshop on Physics at LEP2 [1] that very interesting resutls can be obtained from studying $\gamma\gamma$ events if one or both photons are tagged by the observation of an electron and a positron in the Very Small Angle Tagger (VSAT) detectors. The DELPHI collaboration (see the detailed description of the detector [2]) has already obtained some new results studying the single tag events in the VSAT [3]. Following DELPHI, similar detectors are currently being used in OPAL or are a part of upgrades in ALEPH and L3. The interest in such studies is mainly due to the opportunity they provide to obtain new results in two attractive regions, on the total $\gamma\gamma$ cross

[1]Dept. of Physics, University of Lund, Sweden.
[2]LPNHE, Paris, France.
[3]JINR, Dubna.

section $\sigma_{tot}^{\gamma\gamma}$ and on the so-called P^2 dependence of the photon structure function $F_2^{\gamma}(x, Q^2, P^2)$. The measurement of $\sigma_{tot}^{\gamma\gamma}$ requires both the scattered electron and the positron to be detected by the VSAT while the measurement of the P^2 dependence is possible when one of the scattered leptons is detected by the Small angle TIle Calorimeter (STIC) and another by the VSAT. So in both cases the double tagged mode provides the best possible information about the process, due to the opportunity given to measure both the produced hadronic system and the absolute momentum transfer squared for both photons. The main disadvantage of the double tag mode is limited statistics, due to the small acceptance of detectors used for tag measurements. As a consequence there are some limitations on how to get results with high enough accuracy. In this note we propose the upgrade of the small part of the LEP beam pipe at the VSAT modules which would increase the statistics up to 3.5 times for the VSAT double tags.

2. Apparatus

The VSAT itself is already instrumented to accomodate the larger acceptance. The present scheme of VSAT modules and a simplified geometry of the LEP beam pipe are shown in Fig.1. The VSAT detectors are situated at $\simeq$ 7.7 m from the interaction point, behind the superconducting quadrupole magnets which produce the final focus. These magnets deflect the scattered electrons and positrons from the direction of the beam pipe, and

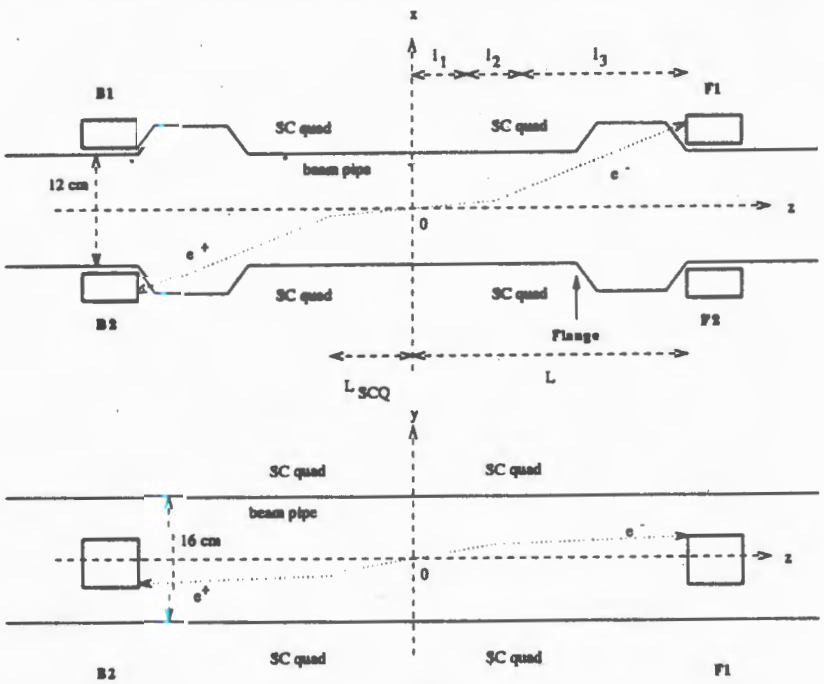

Fig.1. Arrangement of the DELPHI VSAT modules

thus permit measurements at very small polar angles. At the modules there is a small elliptical section ($\simeq$ 60 cm length) of beam pipe providing a thin window in front of the calorimeters. The instrumented area of the VSAT modules is not large, only 5 cm high and 3 cm wide for the x-position measurements (the active area for the calorimeter is 5×5 cm^2). But currently, due to the present construction of the beam pipe, the area used is even smaller, i.e., 2 cm in x-direction, because for the outer range in x of the modules there is a dead zone (see Fig.1) due to a flange in the beam pipe about 70 cm in front of the detectors (see Fig.2). Thus, if a new part of the beam pipe is made with a 1 cm smaller radius in x-direction, the VSAT modules can be moved 1 cm closer to the beam line. This would make the full volume of the detector active allowing us to benefit greatly from the increase in corresponding cross sections, for $\gamma\gamma$ single and double tag measurements, and for the Bhabha scattering processes.

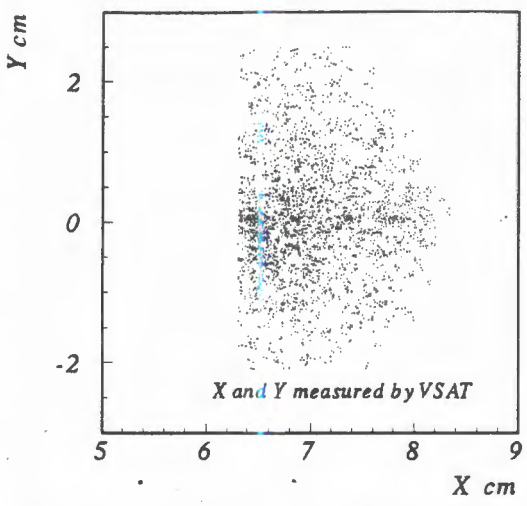

Fig.2. The profile of x and y coordinates measured by the VSAT module in current position

3. Models

Is was shown in our previous study [3] that there is reasonable agreement between DELPHI data and simulation if a so-called QCD-RPC (Resolved Photon Contribution) model is added to the more traditional GVDM and QPM models. The same three-component model is used to obtain an estimate of possible profit for the $\gamma\gamma$ process from the upgrade proposed in LEP2. The standard DELPHI generator is used to simulate Bhabha events. The FASTSIM package together with the standard VSDST program is used to simulate the trajectories of scattered electrons and positrons throughout the DELPHI magnetic field and superconducting quadrupole magnets and to give the response of the VSAT detectors together with all the necessary corrections.

4. Results

When we study the virtuality of the photon structure function $F_2^{\gamma}(x, Q^2, P^2)$, the P^2 is measured by the VSAT only (as a single tagged case), while the Q^2 is measured by the STIC. In the table both the cross sections of single tagged and double tagged modes are estimated. The results are obtained for a LEP2 beam energy of 175 GeV and a 1 cm smaller radius for the LEP beam pipe. Standard criteria to select $\gamma\gamma$ events were applied. Charged particles were accepted if the following criteria were met:

- polar angle from 15° to 165°;
- momentum greater than 0.4 GeV/c.

The event was accepted if the number of charged particles was greater than or equal to 3 with an invariant mass greater than 6 GeV.

One can see that for the double tagged events the statistics available can be increased by a factor 3.5. This is illustrated in Fig.3, where the momentum transfer squared is shown for both the current and new displacements of the VSAT modules. The fact that for the new position the maximum of the distribution is shifted to a lower range can help us also to

Table

Single tagged case				
Models	VDM	QPM	QCD-GS	Total
Current beam pipe	67 pb	9 pb	37 pb	110 pb
Upgraded beam pipe	11 pb	15 pb	63 pb	190 pb
Double tagged case				
Models	VDM	QPM	QCD-GS	Total
Current beam pipe	0.96 pb	0.11 pb	0.61 pb	1.68 pb
Upgraded beam pipe	3.67 pb	0.42 pb	1.79 pb	5.88 pb

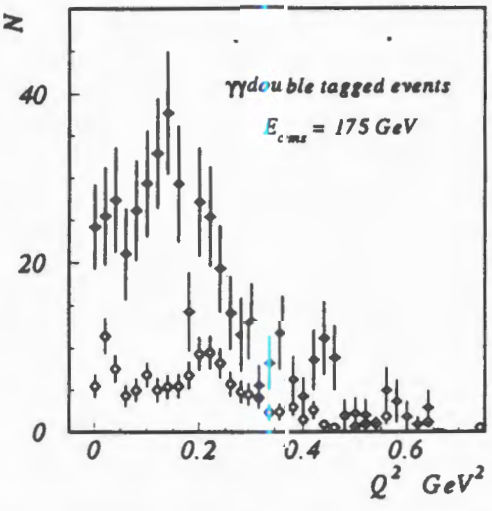

Fig.3. Momentum transfer squared measured by the VSAT detector, in the current position (open circles) and after the upgrade (black circles)

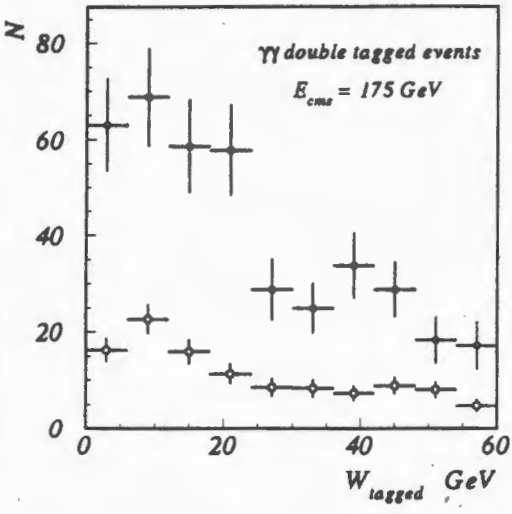

Fig.4. Invariant mass distributions in the current position (open circles) and after the upgrade (black circles)

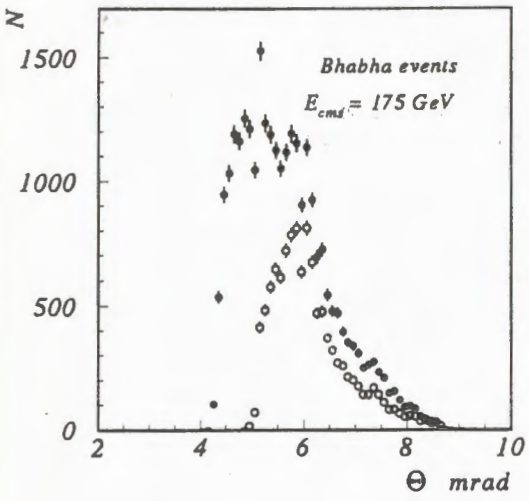

Fig.5. Polar angles measured by the VSAT detector in the current position (open circles) and after the upgrade (black circles)

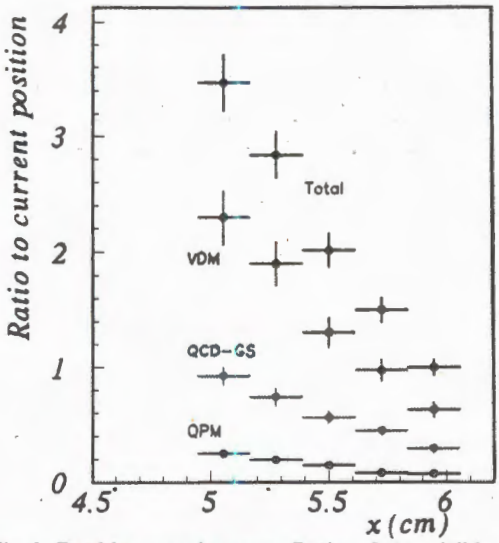

Fig.6. Double tagged events. Ratio of the visible cross section (Total) to the current one (at 6 cm) for smaller displacements in x-direction. Contribution from the VDM, QPM and QCD-RPS (with Gordon-Storrow parameterization) components are also shown

compare results from LEP1 with those from LEP2. It will be possible to find ranges with an overlap of Q^2. Figure 4 shows the invariant mass distribution for both situations. Again it is interesting to note that with the upgrade the statistics can be increased in the higher (more interesting) range of W. Finally, the result for Bhabha events is shown in Fig.5. Here the statistics can also be seen to rise (by a factor of $\simeq 2.5$) together with the angular acceptance ranges in both cases. We believe that the smaller dimension of the beam pipe does not dramatically increase the background of off-momentum electrons. However, it remains to be checked whether such a beam pipe would limit the LEP aperture during injection. If for some reasons a 1 cm smaller radius in x-direction of the LEP beam pipe is unacceptable, the possible profit in statistics for smaller displacement of the VSAT modules (a ratio to the current cross section at 6 cm) is shown in Fig.6. One can see that even 0.5 cm smaller radius arises the statistics for double tagged events by a factor of 2.

5. Conclusions

We have studied hadronic events in simulated two-photon collisions at LEP2 for two positions of the VSAT modules, for the current set-up, and for the new one 1 cm closer to the beam pipe, after a simple upgrade of the LEP beam pipe. It is shown that there will be a considerable increase in statistics with the upgrade proposed.

References

1. Physics at LEP2, CERN 96-01, v.1, p.291.
2. DELPHI Coll., Aarnio P. et al. — Nucl. Instr. and Meth., 1991, v.A303, p.233.
3. DELPHI Coll., Abreu P. et al. — Phys. Lett., 1995, v.B342, p.402.

Received on January 27, 1997.

УДК 621.039.553.5

ESTIMATION OF THE RADIATION ENVIRONMENT AND THE SHIELDING ASPECT FOR THE POINT2 AREA OF THE LHC*

*G.Shabratova, L.Leistam***

The estimation of the radiation environment for the POINT2 of the LHC, where it is planned to locate the ALICE detector, is presented. The dose level and neutron fluences have been studied in the FLUKA-95 and FLUKA-96 framework. The radiation levels have been investigated in the experimental cavern UX25 region, in the machine by-pass areas UL24, US25, UL26 and in the area of the counting rooms PX24. The radiation environment has been studied for two points of accidental beam losses. The dose level in the region of the counting rooms is lower than the recommended CERN limit 50mSv. The radiation level behind the access shielding at the air-duct chicane is not higher than 10mSv that is also appropriated for the use of this area as a public area. A more complicated situation is in the machine by-pass region UL24. The dose level in the tunnel is a few hundreds of mSv as a consequence of a rather small thickness of the separating wall between the shaft and the tunnel (near 1m). The decrease of the radiation level in this region could be achieved by increasing the wall or the beam pipe shielding thicknesses. The latter is more preferable as a cheaper variant.

The investigation has been performed at the Laboratory of High Energies, JINR.

Оценка радиационной обстановки в области пересечения2 LHC и аспекты защиты

Г.Шабратова, Л.Лейстам

Проведена оценка радиационной обстановки в районе пересечения 2 LHC, месте предполагаемого расположения экспериментальной установки ALICE. В рамках моделирующих пакетов FLUKA-95 и FLUKA-96 исследованы дозы радиации и нейтронные потоки. Эти характеристики определялись для экспериментальной зоны UX25, областей обводных машинных каналов UL24, US25, UL26 и района расположения измерительных комнат PX24. Аварийная высадка пучка на элементы вывода рассматривались как источник максимально возможной радиации. Радиационная обстановка была исследована для двух мест таких аварийных ситуаций. Найдено, что уровень доз в районе измерительных комнат не превышает установленного в ЦЕРНе допустимого предела 50 mSv. Уро-

*This work was supported by Engineering Support and Technologies Division of CERN under contract between European Laboratory for Particle Physics and Joint Institute for Nuclear Research.

**European Laboratory for Particle Physics, Geneva, Switzerland

вень радиации за защитой доступа, расположенной рядом с воздухопроводящим каналом области US25, не превышает 10 mSv, что позволяет использовать эту область для свободного доступа персонала. Более сложная ситуация наблюдается в туннеле канала UL24. Здесь доза составляет сотни mSv, что является следствием малой толщины стены, разделяющей шахту основного доступа и туннель. Снижение радиационного уровня в этой области может быть достигнуто увеличением толщины либо этой стены либо защиты, окружающей ионопровод вывода пучка. Последнее предпочтительнее как более дешевый вариант.

Работа выполнена в Лаборатории высоких энергий ОИЯИ.

1. Introduction

The nature of the world and, in particular, the structure of the matter have disturbed the inquisitive part of mankind for a long time. This curiosity initiates the preparation of more complicated and expensive experiments. Nowadays the scientific community hopes that some attractive ideas of high energy physics can be tested with the help of such an experimental facility as a multi-TeV collider. Among these hopes are the discovery of Higgs bosons in p–p interactions and the registration of Quark Gluon Plasma marks in nuclei-nuclei interactions. The creation of large Hadron Collider (LHC) in CERN can be considered as a next effort to provide the first look into the matter at mass scale of 1 TeV. But the operation of such collider at luminosities of 10^{34} cm^{-2}s^{-1} will be confronted by the radiation problems never met before. It is obvious that a thorough understanding of the radiation environment around experiments is required to guide the design of detectors and radiation shieldings.

The human safety is conditioned by the shielding strategy. The investigation of this strategy for the ion-ion experiment at LHC (ALICE) is the main task of the present report.

2. Machine Parameters

The main goal of the ALICE experiment is to study strongly interacting matter at extreme energy densities (QCD thermodynamics) which can be achieved in high-energy heavy-ion collisions. The scientific programme is based on the investigations of central collisions of such heavy nuclei like lead. In addition to the heavy (PbPb) system, the collaboration is planning to study the collisions of lower-mass ions and protons (both pp- and p-nucleus), which provide reference data for nucleus-nucleus collisions [1].

The LHC has been designed to be able to operate as a *proton-proton* and *ion-ion* collider. The energy per charge unit can be maintained at 7 TeV, giving for lead ions $E/A = 2.76$ TeV. The luminosity for these nuclei can reach 1.95×10^{27} cm^{-2}s^{-1}, i.e., almost seven orders of magnitude lower than for $p-p$ beams, 10^{34} cm^{-2}s^{-1} (see the table in Fig.2. with the LHC parameters recommended for radiation calculations [2,3].

The Pb-Pb cross section and average multiplicity are by factors of 35 and 200 larger than the pp ones and both factors decrease the difference between the pp and Pb-Pb radiation background up to three orders of magnitude. On the other hand the maximum

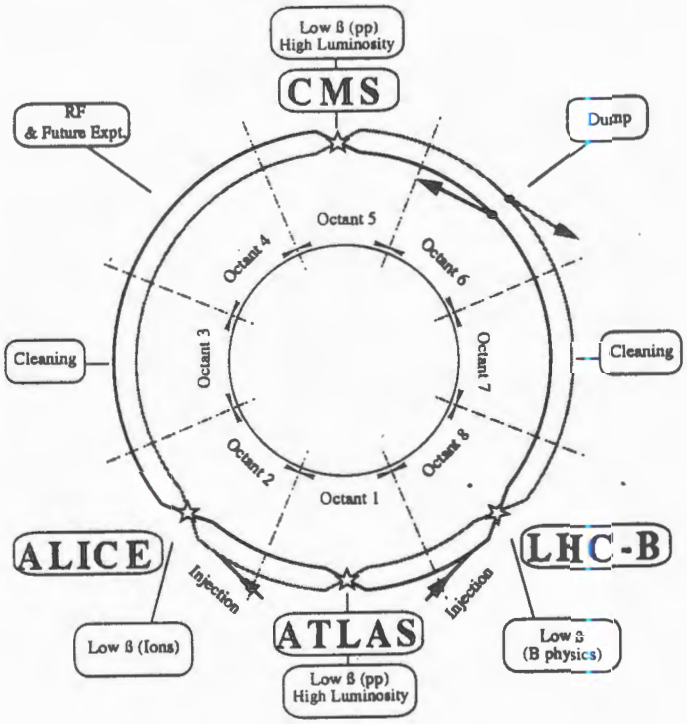

Fig.1. Layout of the LHC machine

Energy per charge E/Q	7 (TeV)
Energy per nucleon E/A	2.76 (TeV)
Peak luminosity L_{pp}	10^{34} ($cm^{-2}s^{-1}$)
PbPb luminosity L_{PbPb}	$(.85 - 1.95)\cdot 10^{27}$ ($cm^{-2}s^{-1}$)
Number of:	
protons per bunch N_b^{pp}	$4.7\cdot 10^{14}$
ions per bunch N_b^{ion}	$(6.3 - 9.4)\cdot 10^{7}$

Fig.2. The LHC parameters

luminosity of *proton-proton* collisions planned for use in the ALICE experiment is about 10^{30} $cm^{-3}s^{-1}$, that is four orders of magnitude lower than in the highest luminosity case, too.

These LHC parameters are very important to estimate a detector radiation load. But for the evaluation of the shielding [4] the accidental loss of a single proton beam is the limiting case.

3. Geometry of the ALICE Location Area

The LHC will be installed in the existing LEP tunnel after the decommisioning of LEP2. A schematic layout of the LHC is shown in Fig.1 [2].

The allocation of the ALICE is planned to be in the second octant of LHC in the region of the so-called Point2 (see Fig.1). This allocation is ideally suited for the detector. As the Point2 experimental area has been designed for the L3 experiment, no significant modifications will be needed for the experimental cavern or the surface zone. Two views of Point2 are shown in Fig.3 and Fig.4. The main access shaft, 23 m in diameter (PX24), has counting rooms. These rooms are separated from the experimental cavern 21.4 m in diameter (UX25) by a large concrete plug 2.4 m in thickness and a concrete screen 1.6 m thick (see Fig.3).

The more severe radiation environment of the LHC requires the reinforcement of the radiation shielding and a modification of a present access situation. A variant of this modification is presented in Fig.4. There are a concrete shielding 1.4 m in thickness

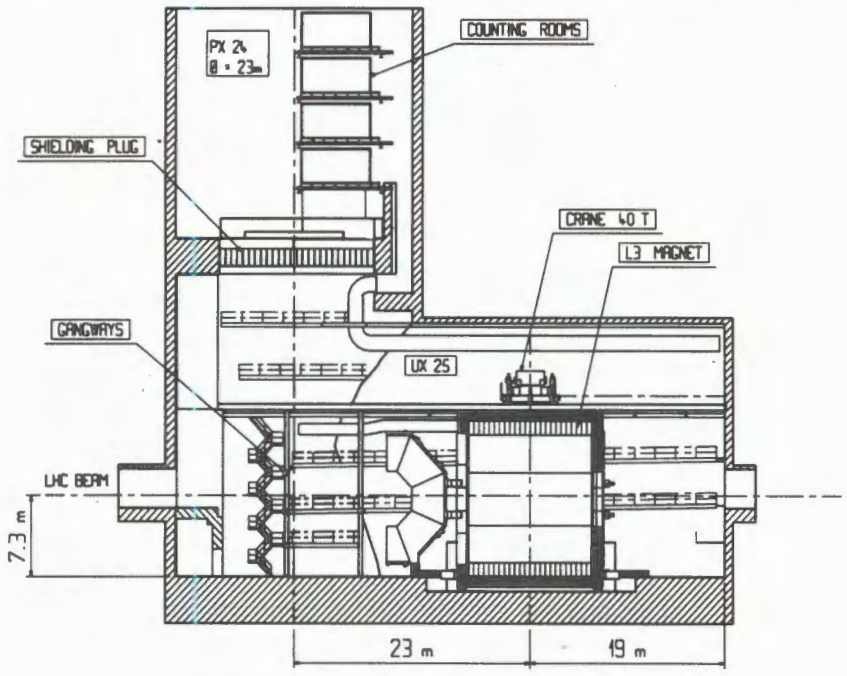

Fig.3. A YZ view of the access shaft and the experimental cavern

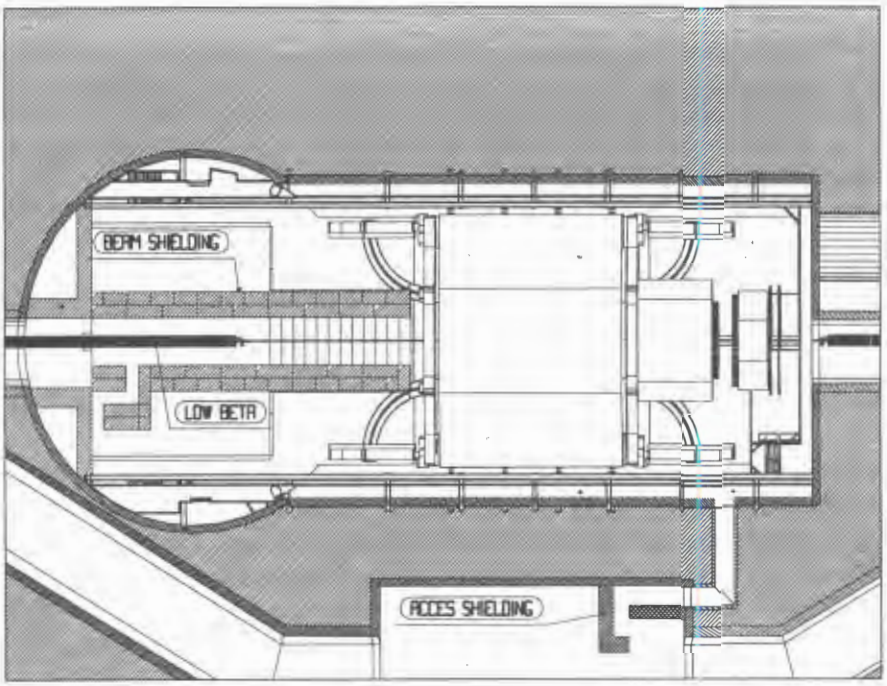

Fig.4. A *XZ* view of the experimental area and the machine by-pass region

surrounding the beam pipe section on the left side from the L3 magnet and concrete screens, called access shielding in Fig.4, at the air-duct chicane communicating the experimental area UX25 and the machine by-pass region (US25) in this modification.

In addition to the described regions there are two tunnels: a left tunnel in the UL24 area and a right one in the UL26 region in Fig.4.

4. Simulation Method

The multipurpose simulation tool named FLUKA (FLUctuating KAskade) [5,6] has been chosen as the most adequate model for the estimation of the radiation environment at LHC.

The cascade propagation through media is developed by this simulation package at a high accuracy level. In the FLUKA Monte-Carlo code [5] high energy interactions are simulated in the framework of the Dual Parton formalism [7]. Interactions at intermediate energies are treated by two distinct models: the resonance production and decay model covers an energy region (1.2-5.0) GeV and the sophisticated pre-equilibrium cascade is developed at energies below 1.3 GeV [8]. The evaporation module uses available nuclear mass and level density tabulations.

The Combinatorial Geometry package allows the accurate tracing of charged particles and Monte-Carlo transport calculations for neutrons and photons. The electromagnetic cascading is prepared by the EMF (Electro Magnetic Fluka) [6] where electrons, positrons and photons can be reliably transported to energies as low as 1-10 KeV. The neutron transport is based on multigroup transport theory using a 72 or 37 group structure [9] and is extended down to thermal energies.

A very accuracy multiple scattering algorithm [10] combined with magnetic field, the photoelectric effect, Compton and Rayleigh inelastic scattering, the pair production, bremsstrahlung, polarization and photonuclear interactions are taken into account in this simulating package.

The benchmark experiments [11,12] have shown that FLUKA is accurate within some tens of percent for dose and fluence estimation. For example, the energy and momentum are exactly conserved within the precision set by a computer (an internal check is set at 10^{-10}).

The important and unique feature of FLUKA is the possibility to use it as a fully analog code, in which case all correlations are presented, or to use any of powerfull variance reduction techniques that are essential for deep penetration studies. The latter can be applied to improve the convergence in some regions of phase space at the cost of others. There are available several techniques: region importance biasing, Russian roulette/splitting in hadronic interactions, leading particles biasing in electromagnetic interactions, non-analog absorption of low energy neutrons and decay length biasing [8].

4.1. *Simulation Conditions.* The geometry of Point2, shown in Figs.3 and 4 is described in terms of FLUKA Combinatorial Geometry. Only L3 magnet has been inserted into the FLUKA geomerty in order to maximize the radiation load of the investigated areas. The main geometric dimensions are shown in Figs.3,4. The sizes of the shielding plug and screen, thickness of the beam pipe shielding are quoted above. In addition to these values, the thickness of each access shielding is chosen to be equal to 80 cm. Thus the total number of volumes used in the FLUKA geometry is equal to 463, and the number of regions — to 995.

As the accidental loss of a single proton beam gives a maximum radiation load of the given regions in our case two points of the proton beam crash have been studied. It is considered in this investigation that only one bunch of $4.7 \cdot 10^{14}$ protons at 7000 GeV (see the table in Fig.2) can initiate such a crash of the LHC machine.

These points are:

— Point *A* is the bunch interaction at $z = -3035$ cm from the meet point of two beams with an iron target 1 m long and 2 cm in radius. This target was placed in the middle of the beam quadrupole;

— Point *B* is an analogous interaction point at $z = 2100$ cm.

The FLUKA95 and FLUKA96 codes were used to simulate the hadronic and electromagnetic cascades generated by primary bunch-target events. These events were simulated in the framework of the DTU JET generator inside the FLUKAS code.

The low limit of kinetic energy for the transport of all produced particles was equal to 10 MeV except antineutrinos and neutral kaons. Thier kinetic energy cut-off was 50 MeV.

The transport of the neutrons of the 72 group structure was switched on, but a detailed transport of electrons, positrons and photons (EMF) was not used. The latter could lead to

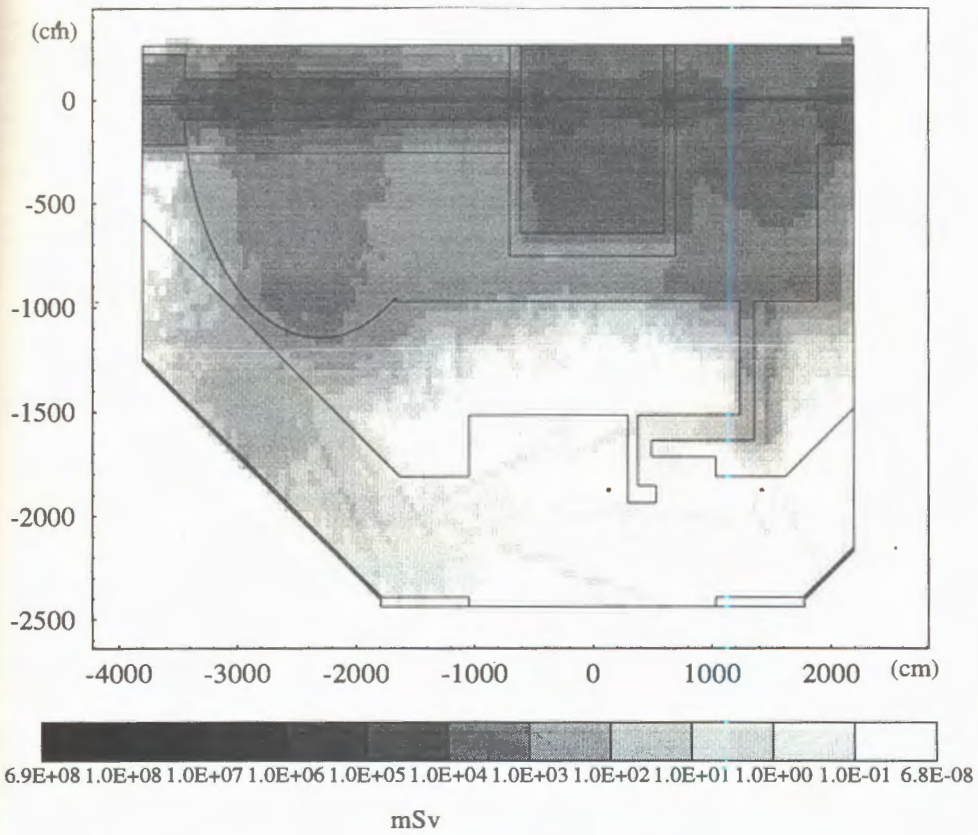

Fig.5. The dose level map for the point *A* in the *XZ* plane

a catastrophic CPU time as the FLUKA geometry of our sample has a huge number of regions mainly connected with dense media. On the other hand we are interested in the dose and neutron fluence in the regions far away from the interaction point, where main contributions are formed by charged hadron and neutron multiplication during their propagation through the matter.

The influence of the L3 magnet field (0.2 *T*) on a radiation load in the regions of our interest is rather weak, but switching on this field during the simulation could lead to a huge increase of the CPU time. For this reason we did not take into account the field of the L3 magnet.

In order to obtain statistically significant results in the investigated areas the following non-analog techniques were used: region importance biasing and Russian roulette/splitting in hadronic interactions. The volumes were divided into subregions or slices with different importance factors proportional to the hadronic mean free path for different regions. The importance increases in the direction of the investigated regions and decreases in the other directions.

The total energy deposition, neutron fluence and track-length were stored. As the main goal of this study is to understand the human safety aspect, the dose result should be

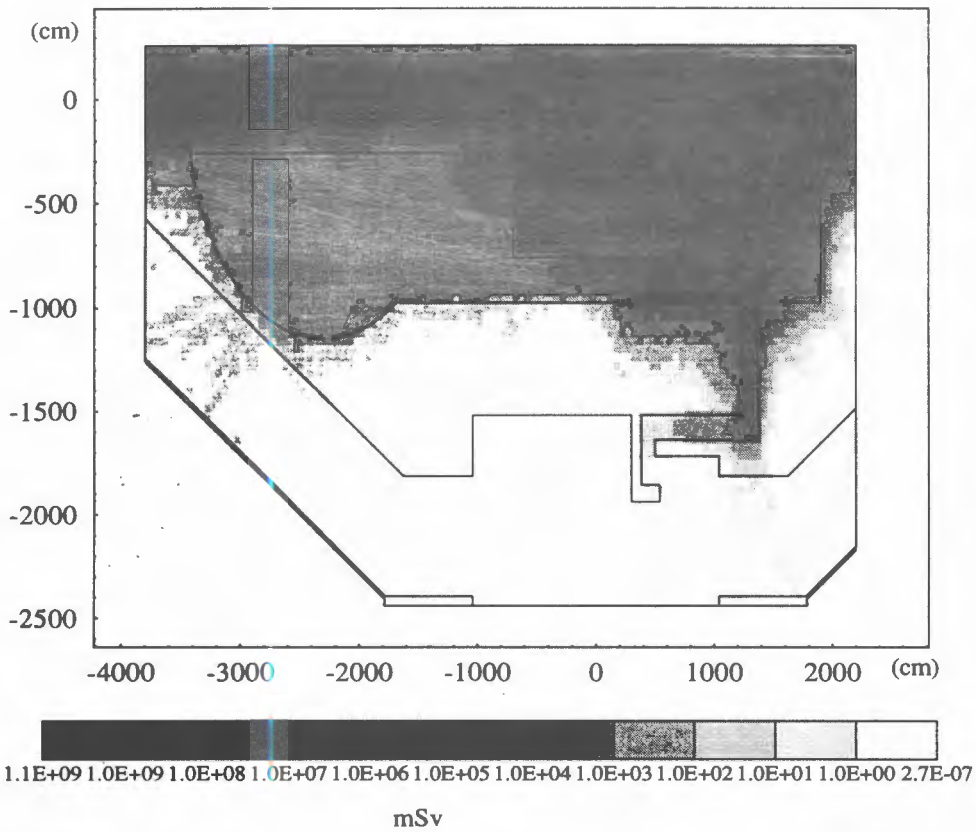

Fig.6. The dose level map for the point *B* in the *XZ* plane

presented in dose equivalent units of *Sv*. The dose equivalent is the absorbed dose weight by the quality factor which is adjusted to reproduce the damage caused in tissue by a given type of radiation. The track-length and energy deposition were weighed by the particle- and energy-dependent fluence to dose conversion factors [13,14].

5. Results

5.1. *Dose Levels.* The dose maps in the *XZ* plane for both points *A* and *B* can be found in Figs.5 and 6.

We shall analyse the radiation environment in the public areas, only.

The most serious situation is observed for the UL24 tunnel. Here the dose level is high as a sequence of rather a small thickness of the separating wall between the shaft and the tunnel (near 1 m). Fig.7 presents a zoom picture of the dose level in this region and Fig.8 shows the dose as a function of the shaft sideway distance inside the UL24 tunnel. It is

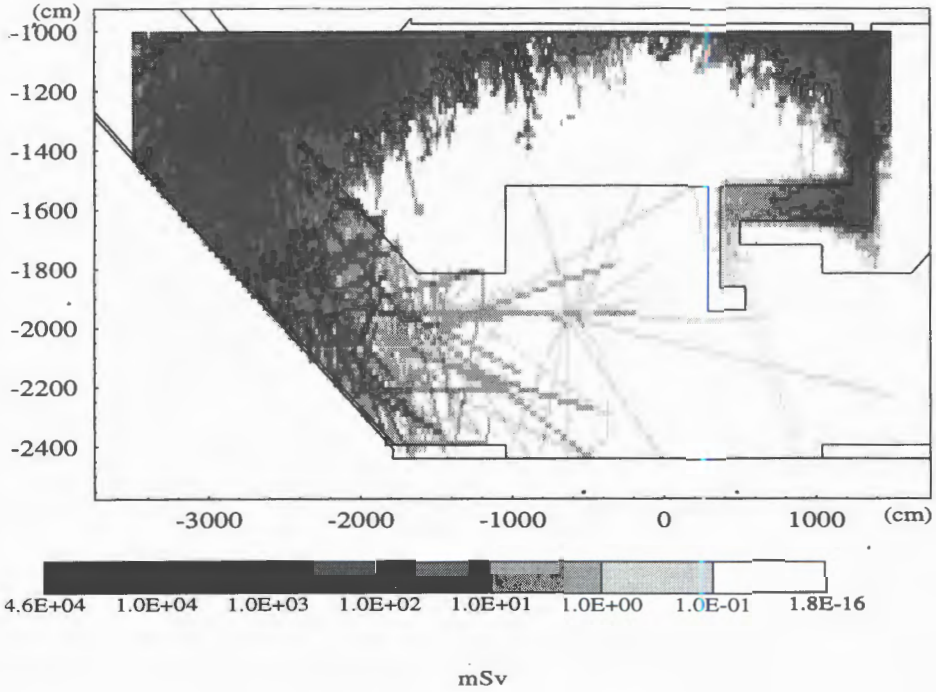

Fig.7. The zoom of the dose level map for point *A*

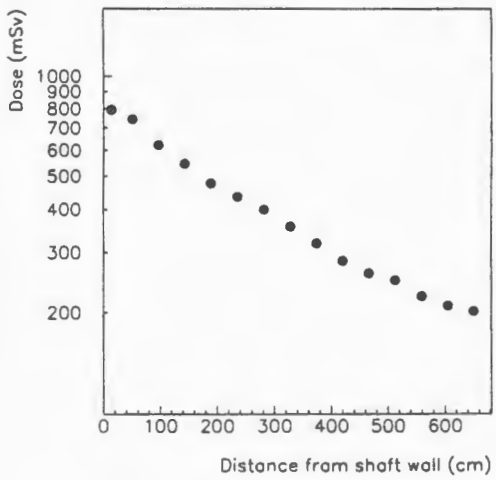

Fig.8. The dose as a function of the shaft sideway distance inside the UL24 tunnel

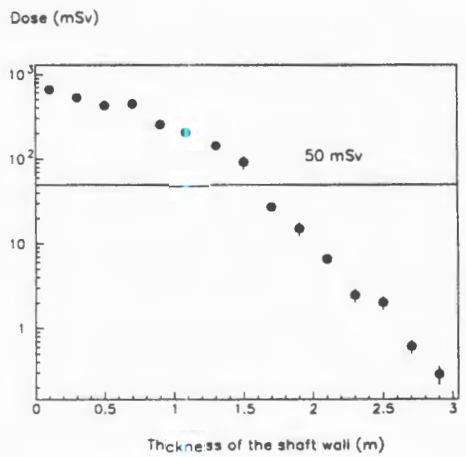

Fig.9. The dependence of the dose on the thickness of the shaft wall at a beam shielding of 2.4 m

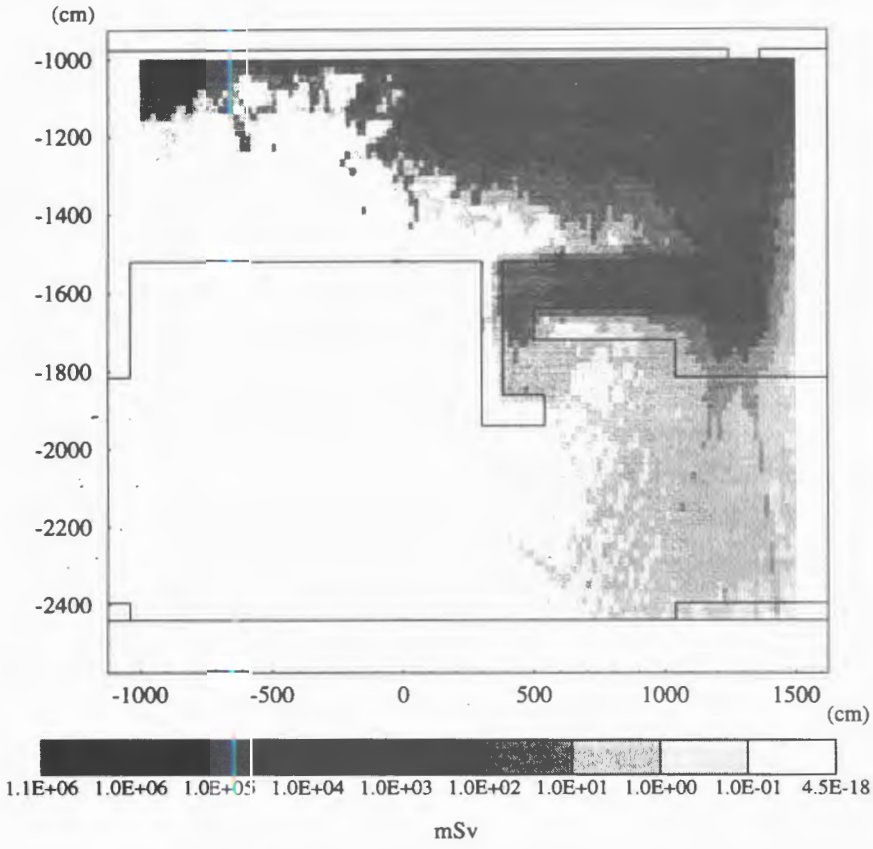

Fig.10. The dose level map for the air-duct chicane region at point *B* in the *XZ* plane

rather a high dose level, which is equal to a few hundreds of mSv in the tunnel. At the point very close to the shaft wall, the dose is a little bit smaller than a thousand mSv. In our earlier report [15], we have shown that a softer situation could be attained by increasing the beam shielding thickness. see Fig.9, where a dose-depth dependence for an infinite wall thichness is presented at a beam shielding thickness of 2.3 m.

The radiation load in the US25 air-duct chicane region behind access shielding is roughly the same for both points (*A* and *B*) and does not exceed 10 mSv. The zoom picture for point *B* is presented in Fig.10. It is obvious, that this area could be used as a public area because the dose is lower than recommended CERN safety limit equal to 50 mSv.

It is seen from Figs.5,6 that the most serious radiation load in the shaft region is observed for point *A*. The dose level in this area is roughly ten times higher than for point *B* case.

Following this conclusion, we present the dose level map in the *XZ* plane only for point *A* in Fig.11. A zoom picture of the area of the most interest, the region of the counting rooms, is depicted in Fig.12. The dose dependences on the plug surface distance for it are

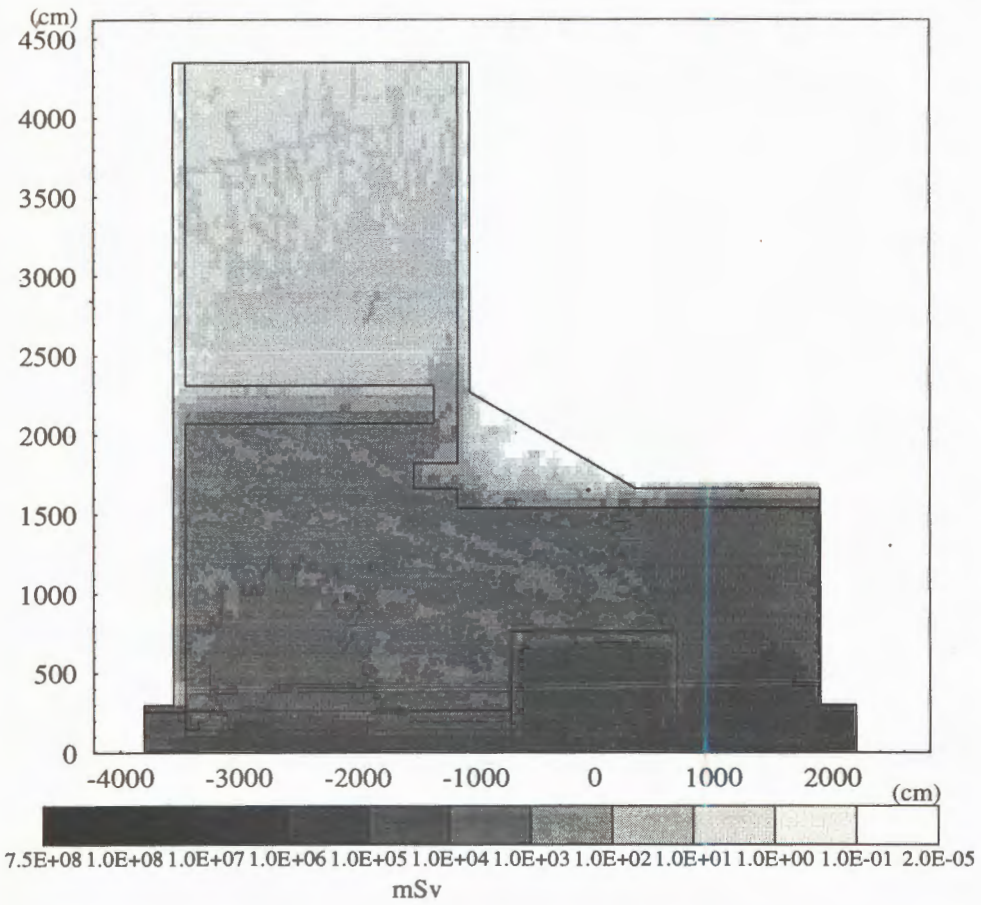

Fig.11. The dose level map for point *A* in the *YZ* plane

in Fig.13. The dependence for the area above the plug is in Fig.13(a) and for the region above the air-duct chicane is in Fig.13(b). It is seen that the dose level in the area of the counting rooms does not exceed the recommended CERN limit, except the regions very close to the chicane. The additional shielding perpendicular to the plug surface (Fig.3) would have to decrease the dose level in this area to a safety level of 50 mSv.

5.2. *Neutron Fluences.* The fluence maps of the neutrons with kinetic energies greater than 100 KeV are shown in Figs.14—16.

The *YZ* view (Fig.14) is given only for point *A* as a map with a greater neutron load. One can see that neutron fluence in the region of the counting rooms does not exceed 10^{12} neutrons per cm^2.

The *XZ* views (Figs.15—16) are presented for the regions of the most interest. The maximum fluence observed in the UL24 tunnel for point *A* (Fig.15) is about $5.0 \cdot 10^{12}$

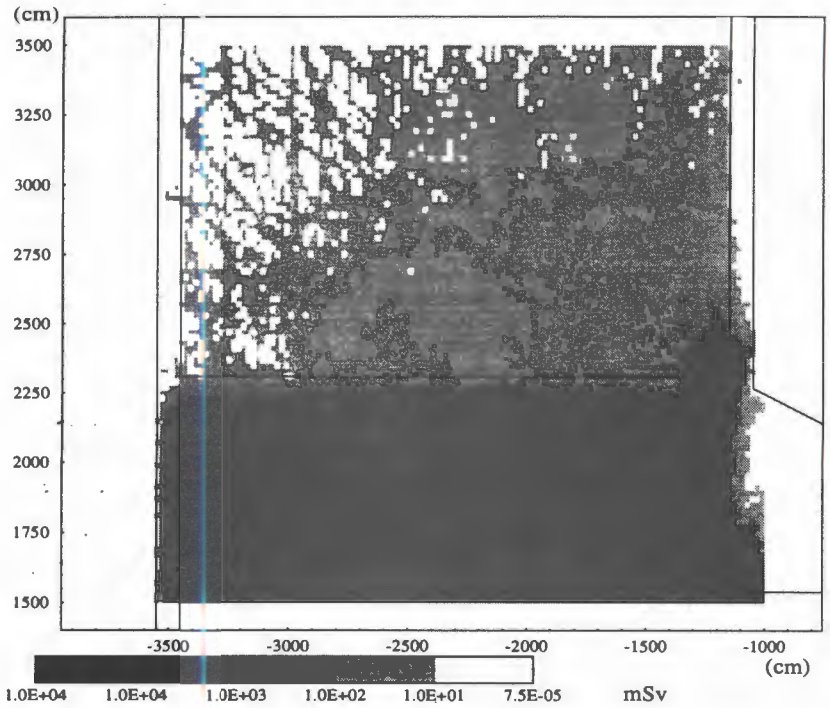

Fig.12. The dose level map in the region of the counting rooms point *A*

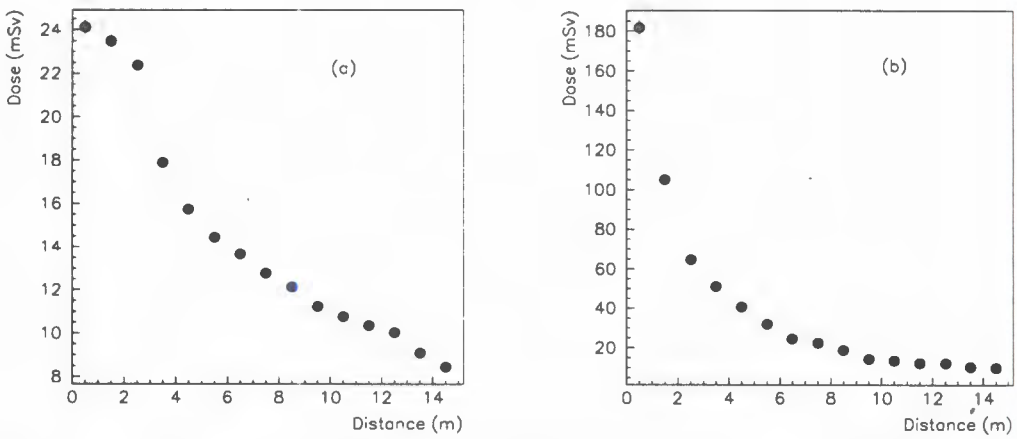

Fig.13. The dose-depth dependence in the counting room area (a) — in the area above the plug surface, (b) — above the air-duct chicane

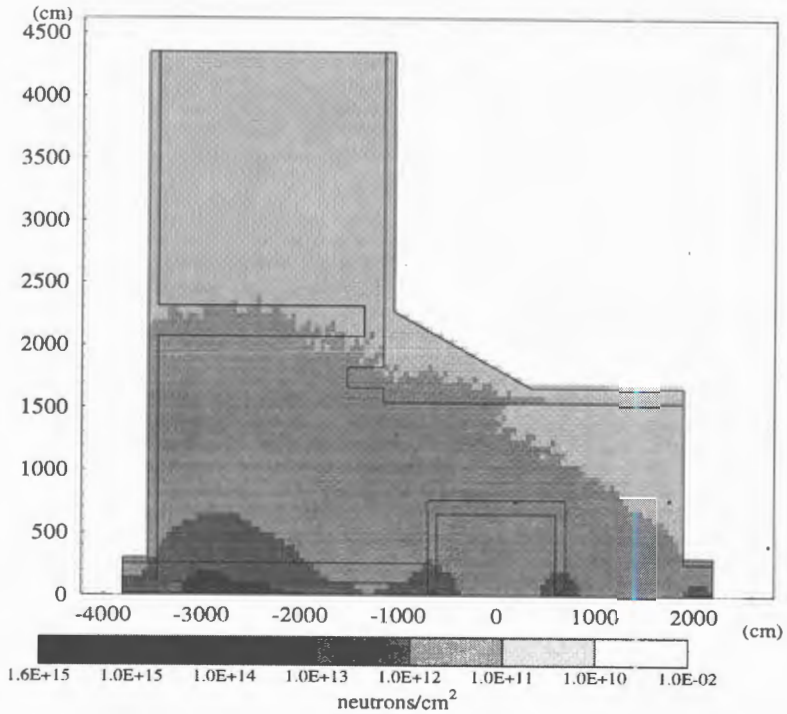

Fig.14. The neutron fluence map for point *A* in the *YZ* plane

neutrons per cm^2. The public area behind the access shielding in the UX25 region for point *B* (Fig.16) has neutron load per cm^2 a little bit greater than 10^{12}.

6. Conclusion

1. It has been found that the dose level in the region of the counting rooms PX24 does not exceed the recommended CERN limit.

2. The radiation level behind the US25 access shielding at the air-duct chicane is not higher than 10 mSv that is also appropriated for the use of this area as a public area.

3. A more complicated situation is in the machine by-pass region of the UL24 tunnel. The dose level in this region is a few hundreds of mSv. The decrease of the radiation load in this region could be achieved by increasing the shaft wall or the beam pipe shielding thickness. The latter is more preferable as a cheaper variant.

4. The fluences of neutron at kinetic energy greater 100 KeV in the public areas do not exceed 10^{13} neutrons per cm^2.

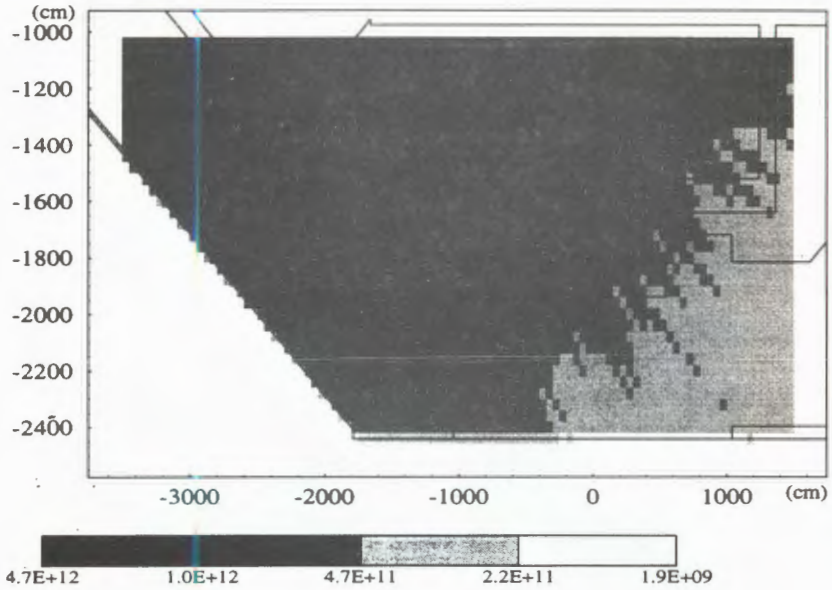

Fig.15. The neutron fluence map for the machine by-pass region, point *A*

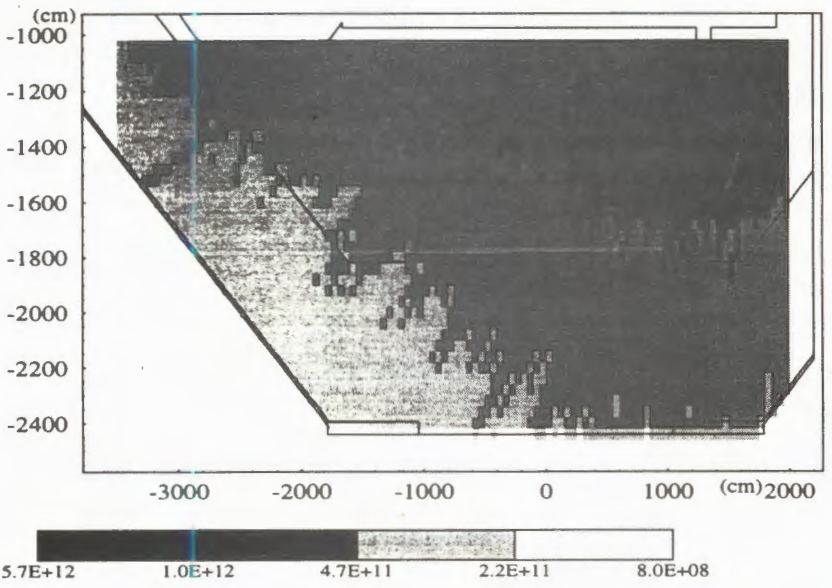

Fig.16. The neutron fluence map for the machine by-pass region, point *B*

Acknowledgements

We would like to thank M.Huhtinen, K.Potter, S.Rollet and G.Stevenson for their help and prolific discussions, A.Vodopianov for constant interest in this work.

References

1. ALICE TP CERN/LHCC 95-71 LHCC/P3.
2. The LHC Study Group, The Large Hadron Collider, Conceptual Design, CERN/AC/95-05(LHC), ed. P.Lefevre and T.Petterson (1995).
3. Hofert M., Potter K., Stevenson G. — CERN/TIS-RP/IR/95-19 (1995).
   Potter K., Stevenson G. — CERN/TIS-RP/IR/95-05.
   Potter K., Stevenson G. — CERN/TIS-RP/IR/95-11.
   Potter K., Stevenson G. — CERN/TIS-RP/IR/95-16.
4. Stevenson G., Hoefert M. — CERN/TIS-RP/IR/94-18.
5. Fasso A., Ferrari A., Ranft J., Sala P.R. — Proc. IV Int. Conf. on Calorimetry in High Energy Physics, La Biodola (Is. d'Elba), Sep. 20—25 1993, ed. A.Menzione and A.Scribano, World Scientific, p.493.
6. Aarnio P. et al. — MC93 Int. Conf. on Monte Carlo Simulation in High Energy and Nuclear Physics, p.88, ed. P.Dragowitscj, S.Linn and M.Burbank, World Scientific, 1994.
7. Capella A., Tran Thanh Van J. — Phys. Lett., 1980, v.93B, p.146.
8. Fasso A., Ferrari A., Ranft J., Sala P. — Specialists' Meeting on Shielding Aspects of Accelerators, Target and Irradiation Facilities, Arlington, Texas, April 28—20, 1994.
9. Ferrari A., Sala P., R.Guaraldi R., Padoani F. — Nucl. Instr. and Meth., 1992, v.B71, p.412.
10. Ferrari A., Sala P. —Nucl. Instr. and Meth., 1992, v.B71, p.412.
11. Fasso A. et al. — Nucl. Instr. and Meth., 1993, v.A332, p.459.
12. Birattari C. et al. — Nucl. Instr. and Meth., 1994, v.A338, p.534.
13. IRCU Report 40 (1986) and ICRP Publication 60, Pergamon Press (1991).
14. Sannikov A.V., Savitskaya E.N. — CERN/TIS-RP/93-14 (1993).
15. Chabratova G., Klempt W., Leistam L., Slavin N. — ALICE/95/41, Internal Note.

Received on April 18, 1997.

УДК 539.18

THE ORTHOPOSITRONIUM DECAY PUZZLE

I.B.Khriplovich*, I.N.Meshkov, A.I.Milstein*

The disagreement between theoretical and experimental values of the orthopositronium decay rate (the lifetime) is described, and possible reasons of its existence are discussed. The new experiment setting-up promising to improve significantly the measurement precision is briefly presented.

The investigation has been performed at the Laboratory of Nuclear Problems, JINR.

Загадка распада ортопозитрония

И.Б.Хриплович, И.Н.Мешков, А.И.Мильштейн

Описывается существующее расхождение теоретического и экспериментального значений времени жизни ортопозитрония, обсуждаются возможные причины этого различия. Кратко представлено предложение новой постановки экспериментов, позволяющей значительно повысить точность измерений.

Работа выполнена в Лаборатории ядерных проблем ОИЯИ.

The strong disagreement between theoretical and experimental values of the orthopositronium decay rate continues to be a «puzzle» of the modern quantum electrodynamics. The theoretical value is [1]

$$\tau_{ortho}^{-1} = \frac{\alpha^6 mc^2}{\hbar}\frac{2(\pi^2-9)}{9\pi}\left[1 - 10.2866(6)\frac{\alpha}{\pi} - \frac{\alpha^2}{3}\ln\alpha^{-1} + B\left(\frac{\alpha}{\pi}\right)^2 - \frac{3\alpha^3}{2\pi}(\ln\alpha^{-1})^2 \ldots\right] =$$

$$= 7.038236(10)\ \mu s^{-1}, \qquad (1)$$

where numerical coefficient B is still under calculation (it requires taking into account numerous two-loop virtual corrections, which is a hard task).

The experimental situation here is not exactly clear. The experiments performed by the University of Michigan group in 1987-90 [2—4], gave the results (see the Table), which exceed essentially the theoretical value. On the other hand, the very recent result of the Tokyo University group [5,6] is consistent, within the experimental accuracy, with the

*Budker Institute of Nuclear Physics, 630090 Novosibirsk, Russia

theoretical value. Clearly, both the theoretical and experimental results are to be examined more carefully.

Table. The theoretical and experimental values of the orthopositronium decay rate

Reference	Year	Decay rate, μs^{-1}	Precision, 10^{-4}	Difference from [1], ms^{-1}
		Theory		
[1]	1992	7.03824(1)	0.01	—
[8,10]	1994	7.04126(12)	0.17	3.02
		Experiment		
[2]	1987	7.0516(13)	1.8	13.36 ± 1.3
[3]	1989	7.0514(14)	1.8	13.16 ± 1.4
[4]	1990	7.0482(16)	2.3	9.96 ± 1.6
[5]	1994	7.0348(80)	5.7	-3.4 ± 8.0
[6]	1995	7.0398(80)	5.7	1.6 ± 8.0

The theoretical uncertainty of the positronium lifetime is related to the coefficient B in formula (1). The problem is that of large second-order corrections. One class of large second-order corrections arises as follows [7]. The large, about -10, factor at the α/π correction to the decay rate (see (1)) means that the factor at the α/π correction to the decay amplitude is roughly -5. Correspondingly, this correction squared contributes about $25(\alpha/\pi)^2$ to the decay rate. Indeed, numerical calculations [8,9] give factor 28.86 at $(\alpha/\pi)^2$ in the contribution.

There is one more class of potentially large contributions to the positronium decay rate. This is relativistic corrections. A simple argument in their favour is that the corresponding parameter $(v/c)^2 \sim \alpha^2$ is not suppressed, as distinct from that of usual second-order radiative corrections, $(\alpha/\pi)^2$, by the small factor $(1/\pi)^2 \sim 1/10$. The relativistic corrections to the positronium decay rate were obtained in [10]. This problem had been addressed previously in [11,12] with different results. The origin of the disagreements was elucidated in [10,13]. The result of the recent paper [14] agrees with [10].

As to the relativistic correction to the parapositronium decay rate, also obtained in Ref.10, its calculation was started by the authors as a warm-up exercise for the much more complicated orthopositronium problem. However, the correction in the singlet case also turns out large, quite close to the sensitivity of the recent experiment [15].

Though the theoretical results indicate that the α^2 correction is very large indeed, it is not sufficiently large to reconcile the theory and experiment [2—4]. As to the experimental result [5,6], its accuracy is still insufficient.

The main limitation of the precision of the experiments is the systematic errors related to the traditional method of positronium generation: positrons are stopped in a target and

recombine then with atomic electrons. New experimental approach will become feasible with the realization of the proposal of the orthopositronium generation, using special storage ring [16,17], and experimental set-up with the fine dericted orthopositronium flux [18]. The proposed scheme promises to obtain the flux of intensity of 10^4 atoms/s with velocity about 0.3 of the speed of light and with very low angular spread — of the order of 1 mrad and the velocity spread of the order of 10^{-4} or less. The peculiarity of the scheme is to use an electron beam, which provides cooling of positrons and, in e^-e^+-recombination, the positronium generation. Thus, the pure vacuum conditions at generation place and in the positronium flux drift channel permit one to reach very low background level. Using Lyman photons as a start signal and γ-quanta from positronium decay as the stop one, we can provide very high precision of the measurements of the orthopositronium lifetime in-flight. One should mention that the velocity spread can limit the measurement accuracy (due to the Lorentz-factor spread) by the value

$$\frac{\Delta\tau}{\tau} \sim \gamma^2\beta^2 \frac{\Delta v}{v} \leq 3\cdot 10^{-6}, \text{ when } \beta \sim 0.2. \qquad (2)$$

This is two orders of magnitude lower of the accuracy level achieved up to now.

Very similar situation takes place in the problem of the parapositronium lifetime. One shoud point out that the proposed scheme with orthopositronium directed flux permits one to perform the experiments on *p–Ps* lifetime measurement with high precision also. For this purpose one can use conversion of *o–Ps* in *p–Ps* mode in external static magnetic or RF-electromangetic field (see details in [18]).

References

1. Adkins G.S., Salahuddin A.A., Schalm K.E. — Phys. Rev., 1992, v.45A, p.777.
2. Westbrook C.I., Gidley D.W., Conti R.S., Rich A. — Phys. Rev. Lett., 1987, v.58, p.1328.
3. Westbrook C.I., Gidley D.W., Conti R.S., Rich A. — Phys. Rev. Lett., 1989, v.A40, p.5489.
4. Nico J.S., Gidley D.W., Rich A., Zitzewitz P.W. — Phys. Rev. Lett., 1990, v.65, p.1334.
5. Asai S., Hyodo T., Hagashima Y., Chang T., Orito S. — Preprint of the University of Tokio, 1994, UT-ICEPP 94-06.
6. Asai S., Orito S., Shinohara N. — Phys. Lett., 1995, v.B357, p.475.
7. Khriplovich I.B., Yelkhovsky A.S. — Phys. Lett., 1990, v.B246, p.520.
8. Burichenko A.P. — Yad. Fiz., 1993, v.56, p.123 [Sov. J. Nucl. Phys., 1993, v.56, p.640].
9. Adkins G.S. — Phys. Rev. Lett., 1996, v.76, p.4903.
10. Khriplovich I.B., Milstein A.I. — Zh. Teor. Fiz., 1994, v.108, p.689 [Sov. Phys. JETP, 1994, v.79, p.379].
11. Kuraev E.A., Kukhto T.V., Silagadze Z.K. — Yad. Fiz., 1990, v.51, p.1638. [Sov. J. Nucl. Phys., 1990, v.51].

12. Labelle P., Lepage G.P., Magnea U. — Phys. Rev. Lett., 1994, v.72, p.2006.
13. Khriplovich I.B., Milstein A.I., hep-ph/9607374.
14. Faustov R.N., Martynenko A.P., Saleev V.A. — Phys. Rev., 1995, v.A51, p.4520.
15. Al-Ramadhan A.H., Gidley D.W. — Phys. Rev. Lett., 1994, v.72, p.1632.
16. Meshkov I.N.., Skrinsky A.N. — Nucl. Instr. and Meth., 1996, v.A379, p.41.
17. Meshkov I.N., Sidorin A.O. — Proc. 11th Int. Workshop on Beam Cooling and Instability Damping, June 18—26, 1996; Nucl. Instr. and Meth., 1997, in print.
18. Meshkov I.N. — Fiz. Elem. Chastits At. Yadra, 1997, v.28, p.495 [Phys. Part. Nucl.].

Received on April 11, 1997.